



A non-Darcy flow model for a non-cohesive seabed involving wave-induced instantaneous liquefaction

Mo-Zhen Zhou^a, Wen-Gang Qi^{b,c,*}, Dong-Sheng Jeng^d, Fu-Ping Gao^{b,c}

^a Key Laboratory for Urban Underground Engineering of the Ministry of Education, Beijing Jiaotong University, Beijing 100044, China

^b Key Laboratory for Mechanics in Fluid Solid Coupling Systems, Institute of Mechanics, Chinese Academy of Sciences, Beijing 100190, China

^c School of Engineering Science, University of Chinese Academy of Sciences, Beijing 100049, China

^d School of Engineering & Built Environment, Griffith University Gold Coast Campus, QLD 4222, Australia

ARTICLE INFO

Keywords:

Nonlinear complementarity problem
Karush–Kuhn–Tucker (KKT) condition
Penalty method
Non-Darcy flow model
Seabed liquefaction
Wave–seabed interactions

ABSTRACT

Prediction of wave-induced instantaneous (oscillatory or momentary) liquefaction is particularly important for the design of offshore foundations. Most previous studies applied the linear Darcy model to characterize the porous flow in a seabed. This treatment was found to cause fallacious tensile stresses in a non-cohesive seabed. In this study, to overcome such shortcomings of previous models, a non-Darcy flow model is proposed based on a Karush–Kuhn–Tucker (KKT) condition. In the KKT condition, the primal constraint arises from the fact that the tensile behavior does not exist in a non-cohesive seabed, while the dual condition arises from the physical evidences that the pore-fluid velocity increases during liquefaction. The non-linearity of the present model is handled by the Newton–Raphson method within the standard finite element framework, without coding constrained variational principle. This highlights the convenience for numerical implementation. The difficulties in treating the nonlinearity by previous dynamic permeability model are also eliminated by the non-Darcy flow model. The merits of the proposed model are validated by examining four numerical treatments and two liquefaction criteria. The liquefaction depth by the present model is found to be roughly 0.73 times of the value by the linear Darcy model.

1. Introduction

For offshore foundations and coastal structures located in the wave-dominated zones, seabed liquefaction associated with wave-induced excess pore pressure is one of key concerns because it threatens the structural stability (Sumer, 2014; Jeng, 2018). The wave-induced seabed liquefaction is also closely associated with sediment erosion or resuspension (Mory et al., 2007; Jia et al., 2014; Zhang et al., 2018b; Tian et al., 2019; Du et al., 2021). In general, the seabed liquefaction can be divided into two categories, based on laboratory experiments and field measurements reported in the literature (Zen and Yamazaki, 1990; Jeng, 2003): (1) the instantaneous liquefaction caused by the transient (or oscillatory) pore pressure; (2) the residual liquefaction caused by the residual (or accumulated) pore pressure. This study focuses on the instantaneous liquefaction in a non-cohesive seabed.

In this scenario, the poro-elasticity assumption can be applied to describe the seabed behavior, because the loose soil has rearranged to a dense state after a long period of ‘wave-induced compaction or solidation’ (Miyamoto et al., 2004; Sumer et al., 2006; Sumer,

2014), making the subsequent wave loading fall into the reloading–unloading stage. The phenomenon of the fluid–seabed interactions has been analytically investigated under various conditions without a structure (Yamamoto et al., 1978; Madsen, 1978; Hsu and Jeng, 1994; Zhang et al., 2013). When a structure is considered, the complicated boundary conditions make the numerical analyses indispensable, such as submarine pipelines (Jeng and Lin, 1999; Gao et al., 2003; Zhao et al., 2014; Zhao and Jeng, 2016; Lin et al., 2016; Duan et al., 2017; Li et al., 2019; Liang et al., 2020; Liang and Jeng, 2021), breakwaters (Jeng et al., 2013; Zhang et al., 2018a; Celli et al., 2019), coastal slopes (Young et al., 2009), offshore wind turbine foundations (Chang and Jeng, 2014; Qi and Gao, 2014; Sui et al., 2016; Lin et al., 2017; Zhao et al., 2017; Li et al., 2018) and immersed tunnels (Han et al., 2019; Chen et al., 2021) etc. The structure–seabed interactions may introduce additional complexities, e.g. the excess pore pressure induced by structure rocking motion (Kudella et al., 2006; Sumer et al., 2008; Cuéllar et al., 2014; Liao et al., 2019), the principal stress rotation (Wang et al., 2017;

* Corresponding author at: Key Laboratory for Mechanics in Fluid Solid Coupling Systems, Institute of Mechanics, Chinese Academy of Sciences, Beijing 100190, China.

E-mail addresses: mzzhou@bjtu.edu.cn (M.-Z. Zhou), qiwengang@imech.ac.cn (W.-G. Qi), d.jeng@griffith.edu.au (D.-S. Jeng), fpgao@imech.ac.cn (F.-P. Gao).

<https://doi.org/10.1016/j.oceaneng.2021.109807>

Received 22 May 2021; Received in revised form 3 August 2021; Accepted 4 September 2021

Available online 14 September 2021

0029-8018/© 2021 Elsevier Ltd. All rights reserved.

Zhu et al., 2019), nonlinear contact behavior at the structure–seabed interface (Qi et al., 2020). Despite that complicated factors have been considered for instantaneous liquefaction, Qi and Gao (2015, 2018) found that existing works can lead to tensile behavior in the liquefied zone. This phenomenon should not occur in a non-cohesive seabed and can lead to a consequence that the liquefaction depths predicted by different liquefaction criteria depart from each other (Qi and Gao, 2015, 2018).

Once this topic is taken into discussion, one can reasonably argue that the porous-medium theory for liquefied soil should be replaced by micro-mechanical discontinuum-based models (Scholtès et al., 2014; Fukumoto and Ohtsuka, 2018; Narsilio et al., 2009; Martin et al., 2020) and then the continuum-based framework for instantaneous liquefaction should be rebuilt. These models motivate the present study to explore the liquefaction mechanism studied from discontinuum-based simulations to present a specified continuum-based model for instantaneous liquefaction. In order to build a bridge from micro scale to engineering scale without expensive computational cost, an alternative approach treating the liquefied soil as a non-Newtonian fluid with a viscosity is proposed (Towhata et al., 1992), in which the liquefied zone should be predetermined. To capture the progressive transition from a two-phase porous medium to a single-phase fluid material, Wang et al. (2020) described the liquefied soil as a thixotropic fluid which was also adopted to describe the non-liquefied soil by changing the model parameters. The difference between the present study and previous investigations is to preserve the two-phase porous-medium assumption for both liquefied and non-liquefied soils. To this end, we need to address the following issue.

If the porous-medium theory is assumed to be still valid for the liquefied soil, the linear elastic assumption could no longer be used. Then, the poro-elastoplastic models (Sassa and Sekiguchi, 2001; Jeng and Ou, 2010; Wang et al., 2014; Ye et al., 2015; Elsafti and Oumeraci, 2016; Wang et al., 2021), which are usually required in the analysis of residual pore pressure, can be applied to analyze the instantaneous liquefaction. However, this extension will pose an ill-condition issue to the global matrix system due to the loss of solid-phase resistance in the liquefied zone. Recently, Zhou et al. (2020b) tried to model the instantaneous liquefaction from a new perspective, i.e. characterizing the fluid-phase flow as a dynamic permeability model instead of the Darcy's law with constant permeability. This treatment preserves the clean poro-elasticity assumption for the solid phase and also avoids handling ill-condition difficulties. The idea is motivated by the literature (Wu and Jeng, 2019; Wu et al., 2020), which characterized the soil permeability k_s being a function of the pore pressure p . The difference is that the previous dynamic permeability model (Wu and Jeng, 2019; Wu et al., 2020) was found to disagree with the permeability increase during soil liquefaction (Arulanandan and Sybico, 1992; Ha et al., 2003; Haigh et al., 2012; Wang et al., 2013; Shahir et al., 2014; Ueng et al., 2017), which was reproduced by Zhou et al. (2020b). Nevertheless, the dynamic permeability model (Zhou et al., 2020b) poses difficulties in nonlinear convergence. Numerical divergence can even occur when using large model parameters or fine computational mesh or simulating the seabed under two-dimensional (2D) wave loading, making the application limited.

To address this issue, Zhou et al. (2021) modeled the instantaneous liquefaction problem in physics as a nonlinear complementarity problem (NCP) in mathematics. The improvements over the dynamic permeability model (Zhou et al., 2020b) are apparent. Within the NCP treatment (Zhou et al., 2021), a Karush–Kuhn–Tucker (KKT) condition is constructed specified for instantaneous liquefaction. It is treated by the Lagrange multiplier method and the primal–dual active set strategy (PDASS) (Kunisch and Rößch, 2002). For the saddle-point system arising from the Lagrange multiplier method, the Direct delta function is used to interpolate the multipliers which can therefore be statically condensed to guarantee the computational efficiency. These treatments, however, are neither standard nor modular within the finite element

framework, making the reproducing effort nontrivial in existing codes (e.g. PORO-FSSI-FOAM, Liang et al. (2020) and Liang and Jeng (2021)). It is therefore not convenient to extend NCP to more general scenarios, e.g. partially-buried pipelines (Zhao and Jeng, 2016; Duan et al., 2017), monopile foundations (Sui et al., 2016; Lin et al., 2017) and gravity foundations for offshore wind turbines (Li et al., 2018).

To minimize the implementation effort and at the same time obtain numerical performances close to the NCP treatment (Zhou et al., 2021), this study establishes a non-Darcy flow model specified for instantaneous liquefaction, on the basis of physical evidences (e.g., micro mechanisms, laboratory experiments and field trials). In order to avoid any unnecessary misleading of the existing non-Darcy models determining the limits of Darcy's law validity by means of Reynolds number (e.g. Forchheimer model Girault and Wheeler, 2008, Hansbo model Hansbo, 2001), it is clarified here that the present model is derived based on a new concept, wherein the liquefaction criterion is revised as a primal constraint based on micro-scale simulations and field observations. The primal constraint is first imposed by the Lagrange multiplier method to make clear the physical meaning of the Lagrange multiplier, so as to find a dual complementarity condition to check and then correct the assumed liquefied zone. The primal–dual pair forms a Karush–Kuhn–Tucker (KKT) condition, removing the requirement that the liquefied zone should be predetermined (Towhata et al., 1992).

It is noted that the KKT condition is a mathematical concept within non-linear complementarity problem (NCP). It was previously applied to model multi-body contact behavior (Wriggers, 2006; Popp et al., 2013; Zhou et al., 2018), multiple cracks (Zheng et al., 2015) and the non-associative plasticity with non-smooth yield surfaces (Zheng et al., 2020) etc. Motivated by these works, Zhou et al. (2021) presented a KKT condition for instantaneous liquefaction and treated the KKT condition by constrained variational principle. In this work, we construct a new type of KKT condition that is different from the KKT condition presented in Zhou et al. (2021). Furthermore, by means of the penalty method and variational equivalence, the KKT condition constructed here turns out to be clear in physics as a concise non-Darcy formulation, which can be conveniently treated by the standard Newton–Raphson method. Thus, the implementation effort becomes trivial, due to that coding constrained variational principle for NCP, as implemented in Zhou et al. (2021), is no longer required. The difficulties of the dynamic permeability model (Zhou et al., 2020b) in nonlinear convergence are also well addressed by the new non-Darcy model.

Without losing rigorousness in mathematics, Section 2 starts from the construction of NCP and its weak forms by using Lagrange multiplier method and penalty method, respectively. The physical evidences for the primal constraint are also provided in this section. By modeling the NCP as a non-Darcy flow model, Section 3 provides the physical evidences for the dual condition. Exemplary results are provided under one-dimensional (1D) and 2D wave loading conditions in Sections 4 and 5, confirming that the nonlinear convergence of the present model is superior. Two liquefaction criteria widely applied in ocean engineering are discussed in detail and found to become unified by the new model. Effects of the soil and wave parameters as well as the penalty parameter introduced by the non-Darcy model are also investigated. Finally, several conclusions are drawn in Section 6.

2. Nonlinear complementarity problem arising from instantaneous liquefaction

2.1. Basis of wave–seabed interactions and liquefaction criteria

Fig. 1 shows the wave–seabed interactions and associated seabed liquefaction, wherein the seabed thickness, water depth and wave height are denoted by d , h and H , respectively. The coordinate z equals to zero at the seabed surface and all the other positions in seabed

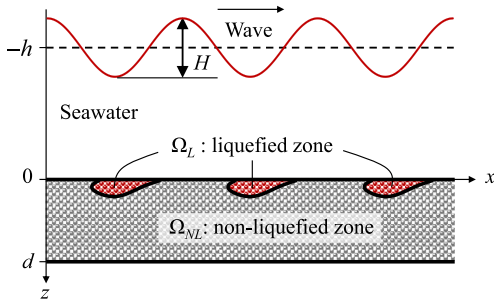


Fig. 1. Schematic of the wave-seabed interactions involving instantaneous liquefaction.

correspond to positive values of z . Note that the wave is shown as linear in Fig. 1. If large waves in shallow water are involved, then Stokes wave (Gao et al., 2003) or cnoidal wave (Zhou et al., 2014) should be applied to account for the nonlinear effect. For simplicity, the linear wave theory (Dean and Dalrymple, 1984) is applied in this study:

$$P_b = p_0 \cos\left(\frac{2\pi}{L}x - \frac{2\pi}{T}t\right), \quad (1)$$

where P_b is the periodic wave pressure applied at the seabed surface, i.e. $z = 0$. The amplitude of P_b is denoted by p_0 . L and T denote the wavelength and wave period, respectively. L and p_0 are determined by:

$$L = \frac{gT^2}{2\pi} \tanh\left(\frac{2\pi h}{L}\right), \quad p_0 = \frac{\gamma_w H}{2 \cosh(2\pi h/L)}, \quad (2)$$

where g is the acceleration of gravity and γ_w is the weight of water per unit volume.

When instantaneous liquefaction occurs, the considered seabed domain Ω is decomposed into two non-overlapping sub-domains:

$$\Omega = \Omega_L \cup \Omega_{NL}, \quad \Omega_L \cap \Omega_{NL} = \emptyset. \quad (3)$$

where Ω_L and Ω_{NL} denote the instantaneously liquefied and non-liquefied zones, respectively.

The liquefied zone (Ω_L) can be determined by several criteria, among which two criteria widely applied in ocean engineering are as follows (Qi and Gao, 2018):

$$p - P_b \geq \gamma' z, \quad (4)$$

$$j_z \geq \gamma', \quad (5)$$

where p is the wave-induced excessive pore pressure. Its gradient along the vertical direction is denoted by $j_z = \partial p / \partial z$. γ' is the buoyant unit weight of the seabed and can be determined by: $\gamma' = (G_s - 1)(1 - n)\gamma_w$, where G_s is the specific gravity of sand particles and n is the sand porosity. The porosity n has a relation with the void ratio e (the ratio of the void volume to the volume of solid particles): $n = e/(1+e)$.

The criterion by Eq. (4) was deduced by Zen and Yamazaki (1990), based on the force analysis on the vertical soil column. When wave trough arrives, the excess pore pressure p and the wave pressure P_b become both negative. Instantaneous liquefaction occurs when the difference $p - P_b$ exceeds the overburden seabed pressure $\gamma' z$. The extension of this criterion to three-dimensional scenarios was presented by Jeng (1997).

The criterion by Eq. (5) was proposed by Bear (1972) from the perspective of soil-element scale. The positive value of j_z can be interpreted as the upward seepage force. If the upward seepage force exceeds the critical value (usually chosen as γ'), the soil layer will reach a instantaneously-liquefied state.

2.2. Revising the liquefaction criterion as a primal constraint

Generally, the liquefied zones determined by the above two criteria can be different. This issue was recently discussed by Qi and Gao (2018) and was found to be caused by the tensile behavior occurring in Ω_L . This phenomenon was stated as nonphysical (Qi and Gao, 2018), according to the evidences shown in Fig. 2.

The first evidence is the temporal effective stress obtained by the simulations using the discrete element method (DEM) coupled with a pore-scale finite volume (PFV) scheme (Scholtès et al., 2014), as presented in Fig. 2(a). The effective stress by the numerical simulations stays non-negative even liquefaction occurs. The micro-mechanical investigation of liquefaction of granular media by cyclic DEM tests (Martin et al., 2020) produces similar conclusions. This motivates revising the liquefaction criterion by Eq. (4) as the following primal constraint:

$$p - P_b = \gamma' z \quad \text{in } \Omega_L. \quad (6)$$

The second evidence is the field trials by Mory et al. (2007) wherein 47 instantaneous liquefaction events were observed, as shown in Fig. 2(b). Despite that the wave height varies from 0.75 m to 1.8 m, the upward seepage force (j_z) generally approximates to a threshold value, i.e. the buoyant unit weight (γ'). A further increase of wave height could not induce higher seepage force in the liquefied zone. This motivates revising the liquefaction criterion by Eq. (5) as the following primal constraint:

$$j_z = \gamma' \quad \text{in } \Omega_L. \quad (7)$$

Eq. (6) has been numerically handled by Zhou et al. (2021). This study focuses on dealing with the primal constraint by Eq. (7) in a numerical manner. With Eq. (7) as an additional constraint, the boundary value problem can be given as:

$$\nabla \cdot (\sigma' - p \mathbf{I}_{2 \times 2}) + \mathbf{b} = 0 \quad \text{in } \Omega, \quad (8a)$$

$$\frac{\partial \epsilon_v}{\partial t} + n\beta \frac{\partial p}{\partial t} - \nabla \cdot \left(\frac{k_s}{\gamma_w} \nabla p \right) = 0 \quad \text{in } \Omega, \quad (8b)$$

$$j_z = \gamma' \quad \text{in } \Omega_L, \quad (8c)$$

$$\mathbf{u} = \hat{\mathbf{u}} \quad \text{on } \Gamma_u, \quad (8d)$$

$$\sigma \cdot \mathbf{n}_\sigma = \hat{\mathbf{t}} \quad \text{on } \Gamma_\sigma, \quad (8e)$$

$$p = \hat{p} \quad \text{on } \Gamma_p, \quad (8f)$$

$$\mathbf{v}_w \cdot \mathbf{n}_v = \hat{v}_w^n \quad \text{on } \Gamma_v. \quad (8g)$$

where the former two equalities arise from the poro-elastic theory (Biot, 1941) and represent the equilibrium of the solid-fluid mixture and the conservation of mass, respectively. In Eq. (8a), σ' is the effective stress, $\mathbf{I}_{2 \times 2}$ is a second-order unit tensor and \mathbf{b} is the body force per unit volume. In Eq. (8b), ϵ_v is the volumetric strain, t denotes time, β is the pore fluid compressibility and k_s is the Darcy's coefficient of permeability. The pore fluid compressibility is determined by (Verruijt, 1969):

$$\beta = \frac{1}{K_{w0}} + \frac{1 - S_r}{P_{abs}}, \quad (9)$$

where K_{w0} is the true bulk modulus of pore water and can be taken as 2.0×10^9 Pa (Yamamoto et al., 1978). S_r denotes the degree of saturation and P_{abs} is the absolute water pressure.

The latter four equalities in Eq. (8) represent the boundary conditions. Γ_u and Γ_σ are Dirichlet and Neumann boundaries of the solid phase, respectively. In Eq. (8d), \mathbf{u} is the displacement vector and $\hat{\mathbf{u}}$ is

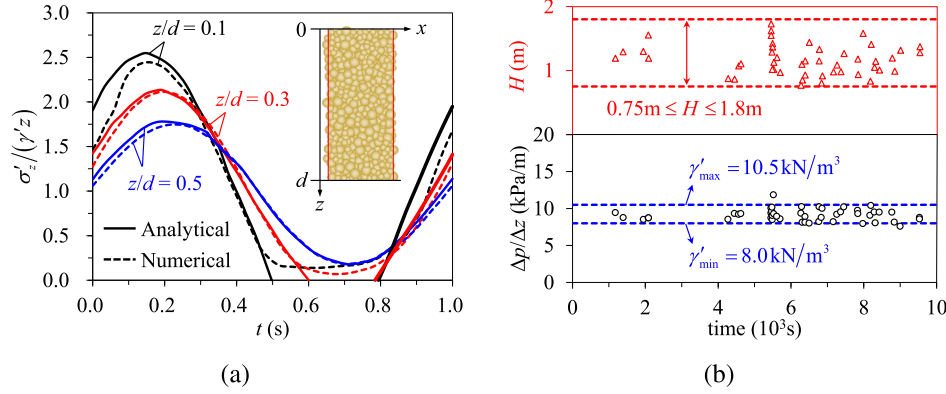


Fig. 2. Evidences for the primal constraints: (a) DEM-PFV simulations (Scholtès et al., 2014); (b) field trials (Mory et al., 2007).

the constrained displacement. In Eq. (8e), σ is the total stress tensor, \mathbf{n}_σ is the outward unit normal vector of Γ_σ and $\hat{\mathbf{t}}$ is the boundary traction. Γ_p and Γ_v are Dirichlet and Neumann boundaries of the fluid phase, respectively. In Eq. (8f), \hat{p} is the constrained pore pressure. In Eq. (8g), \mathbf{v}_w is the pore-fluid velocity vector, \mathbf{n}_v is the outward unit normal vector of Γ_v and \hat{v}_w^n denotes the boundary Darcy velocity.

2.3. Finding the dual condition complementary to the primal constraint

The primal constraint in Eq. (8) is still insufficient to obtain expected results, because the liquefied zone Ω_L is undetermined as well as time-dependent. Therefore, a dual condition is needed to check and then correct Ω_L . To this end, the Lagrange multiplier method is used to impose the primal constraint, with the Lagrange multiplier λ introduced as an additional unknown field. The trial and weighting spaces are defined as:

$$\mathcal{V}_u = \left\{ \mathbf{u} \in [H^1(\Omega)]^3 \mid \mathbf{u}|_{\Gamma_u} = \hat{\mathbf{u}} \right\}, \quad \mathcal{V}_\Phi = \left\{ \Phi \in [H^1(\Omega)]^3 \mid \Phi|_{\Gamma_u} = \mathbf{0} \right\}, \quad (10a)$$

$$\mathcal{V}_p = \left\{ p \in [H^1(\Omega)] \mid p|_{\Gamma_p} = \hat{p} \right\}, \quad \mathcal{V}_\phi = \left\{ \phi \in [H^1(\Omega)] \mid \phi|_{\Gamma_p} = 0 \right\}, \quad (10b)$$

$$\mathcal{V}_\lambda = \left\{ \lambda \in [H^1(\Omega)] \mid \lambda|_{\Omega_{NL}} = 0 \right\}, \quad (10c)$$

$$\mathcal{V}_w = \left\{ w \in [H^1(\Omega)] \mid w|_{\Omega_{NL}} = 0 \right\},$$

where H^1 is a Sobolev space of degree one. Φ , ϕ and w are variations of \mathbf{u} , p and λ , respectively.

The weak form can therefore be stated as finding $(\mathbf{u}, p, \lambda) \in \mathcal{V}_u \times \mathcal{V}_p \times \mathcal{V}_\lambda$ such that there holds:

$$\int_{\Omega} \nabla \Phi : (\sigma' - p \mathbf{I}_{2 \times 2}) \, d\Omega + \int_{\Omega} \Phi \cdot \mathbf{b} \, d\Omega + \int_{\Gamma_\sigma} \Phi \cdot \hat{\mathbf{t}} \, d\Gamma = 0, \quad (11a)$$

$$\int_{\Omega} \phi \left(\frac{\partial \varepsilon_v}{\partial t} + n\beta \frac{\partial p}{\partial t} \right) \, d\Omega + \int_{\Omega} \frac{k_s}{\gamma_w} \nabla \phi \cdot \nabla p \, d\Omega + \int_{\Gamma_v} \phi \hat{v}_w^n \, d\Gamma + \int_{\Omega_L} \frac{\partial \phi}{\partial z} \lambda \, d\Omega = 0, \quad (11b)$$

$$\int_{\Omega_L} w \left(\frac{\partial p}{\partial z} - \gamma' \right) \, d\Omega = 0, \quad (11c)$$

for all $(\Phi, \phi, w) \in \mathcal{V}_\Phi \times \mathcal{V}_\phi \times \mathcal{V}_w$.

Eq. (11c) is the weak form of the primal constraint Eq. (7). Eq. (7) further introduces another additional variational term into the weak form, i.e. the last term in Eq. (11b). This term represents the virtual work in the liquefied zone contributed by the Lagrange multiplier (λ),

whose physical meaning can therefore be presented as a fictitious pore-fluid velocity. Existing works found that soil liquefaction can speed up the pore-fluid flow and regarded this phenomenon as the permeability increase. Among these, Arulanandan and Sybico (1992) reported that the sand permeability during liquefaction increased to 6–7 times its initial value. The permeability was observed by Haigh et al. (2012) to increase 1.1–5 times the original value, as the effective stress approached zero. Other studies indicated the ratio of permeability during liquefaction to its initial value as 1.4–5 (Ha et al., 2003), 4 (Wang et al., 2013), or 4–5 (Ueng et al., 2017), etc. This motivates constructing the dual complementary condition as follows:

$$\lambda \geq 0 \quad \text{in } \Omega_L. \quad (12)$$

The above equation means that the additional pore-fluid velocity (λ) should be non-negative in the liquefied zone, so as to help the excessive pore pressure decreasing appropriately in an implicit manner such that tensile behavior never occurs. Now that the primal constraint ($j_z = \gamma'$) and its dual condition ($\lambda \geq 0$) have been obtained for the liquefied zone, the KKT condition for instantaneous liquefaction can therefore be given as:

$$j_z \leq \gamma', \quad \lambda \geq 0, \quad (j_z - \gamma') \lambda = 0, \quad \text{in } \Omega, \quad (13)$$

2.4. Weak form by using the penalty method

The penalty method (Meng and Yang, 2010) is another classic technique for imposing the KKT condition. Compared with the Lagrange multiplier method, the penalty method imposes the constraints in an approximate manner but is more convenient for numerical implementation. With the use of this method, a penalty factor κ is introduced to build a connection between the primal and dual variables. The KKT condition by Eq. (13) is then rewritten as a penalized form:

$$\lambda = \kappa (j_z - \gamma'), \quad \text{with } \kappa = \begin{cases} 0, & \text{if } j_z < \gamma' \\ \kappa_\infty, & \text{if } j_z \geq \gamma' \end{cases}, \quad (14)$$

where κ_∞ is the penalty parameter used in the liquefied zone. If κ_∞ equals to ∞ , Eq. (14) is equivalent to Eq. (13). However, ∞ is not possible to achieve during the numerical procedure and hence κ_∞ is usually chosen as a large value. Eq. (14) is an approximate version of Eq. (13). The subscript ∞ is used here to keep in mind that κ_∞ should be large enough to make the original KKT condition be approximated with satisfactory accuracy.

By using the primal–dual relationship given by Eq. (14), the weak form by using the Lagrange multiplier method, Eq. (11), can then be rewritten as:

$$\int_{\Omega} \nabla \Phi : (\sigma' - p \mathbf{I}_{2 \times 2}) \, d\Omega + \int_{\Omega} \Phi \cdot \mathbf{b} \, d\Omega + \int_{\Gamma_\sigma} \Phi \cdot \hat{\mathbf{t}} \, d\Gamma = 0, \quad (15a)$$

$$\begin{aligned} \int_{\Omega} \phi \left(\frac{\partial \varepsilon_v}{\partial t} + n\beta \frac{\partial p}{\partial t} \right) d\Omega + \int_{\Omega} \frac{k_s}{\gamma_w} \nabla \phi \cdot \nabla p d\Omega \\ + \int_{\Gamma_v} \phi \hat{v}_w^n d\Gamma + \int_{\Omega} \kappa \frac{\partial \phi}{\partial z} \left(\frac{\partial p}{\partial z} - \gamma' \right) d\Omega = 0. \end{aligned} \quad (15b)$$

It can be found that the primal constraint explicitly represented as Eq. (11c) by using the Lagrange multiplier method is now implicitly determined here by the penalty factor κ .

3. Reformulating the nonlinear complementarity problem as a non-Darcy flow model

In the above section, either Eq. (11) or Eq. (15) can be adopted to find the solution (\mathbf{u}, p) . However, the constrained variational principle may lead to barriers for numerical implementation and future extensions, because it is neither standard nor modular within the finite element framework. In order to provide a numerical formulation easier to be reproduced, this section reformulates the above penalty formulation (Eq. (15)) as an equivalent non-Darcy flow model.

3.1. Weak form with nonlinear flow

If nonlinear relation between the velocity and the pressure gradient is considered, then the mass conservation equation, Eq. (8b), must be modified as:

$$\frac{\partial \varepsilon_v}{\partial t} + n\beta \frac{\partial p}{\partial t} + \nabla \cdot \mathbf{v}_w = 0 \quad \text{in } \Omega. \quad (16)$$

The weak form by using nonlinear flow is then given as follows:

$$\int_{\Omega} \nabla \Phi : (\sigma' - p \mathbf{I}_{2 \times 2}) d\Omega + \int_{\Omega} \Phi \cdot \mathbf{b} d\Omega + \int_{\Gamma_\sigma} \Phi \cdot \hat{\mathbf{t}} d\Gamma = 0, \quad (17a)$$

$$\int_{\Omega} \phi \left(\frac{\partial \varepsilon_v}{\partial t} + n\beta \frac{\partial p}{\partial t} \right) d\Omega - \int_{\Omega} \nabla \phi \cdot \mathbf{v}_w d\Omega + \int_{\Gamma_v} \phi \hat{v}_w^n d\Gamma = 0. \quad (17b)$$

3.2. Non-Darcy flow model arising from the nonlinear complementarity problem

Keeping in mind that the non-Darcy model is a variationally equivalent version of the penalized KKT condition, Eq. (17b) should be identical to Eq. (15b). That is, the second term in Eq. (17b) should equal to the sum of second and last terms in Eq. (15b). This equivalence provides the following function to determine the pore-fluid velocity \mathbf{v}_w :

$$v_{wx} = -\frac{k_s}{\gamma_w} \frac{\partial p}{\partial x}, \quad v_{wz} = -\frac{k_s}{\gamma_w} \frac{\partial p}{\partial z} - \kappa \left(\frac{\partial p}{\partial z} - \gamma' \right), \quad (18)$$

where v_{wx} and v_{wz} are the two components of \mathbf{v}_w in the horizontal and vertical directions, respectively. In Eq. (18), the Darcy's law still holds in the horizontal direction, while an apparent non-linearity arising from the penalty factor κ appears in the vertical direction.

According to Eq. (14), it is known that the second term in v_{wz} in Eq. (18) is the Lagrange multiplier λ . Therefore, the actual pore-fluid velocity in Ω_L contains two parts, with one coming from the conventional Darcy's law and the other λ . This makes clear again that the Lagrange multiplier λ means the additional pore-fluid velocity added into Ω_L . Noting that the pressure gradient has a relation to the hydraulic gradient ($\Delta p = \gamma_w i$), v_{wz} can be rewritten in terms of i_z :

$$v_{wz} = -k_s i_z - \kappa (i_z - i_{cr}) = \begin{cases} -k_s i_z, & \text{if } i_z < i_{cr} \\ -k_s i_{cr} - (k_s + \kappa_\infty \gamma_w) (i_z - i_{cr}), & \text{if } i_z \geq i_{cr}, \end{cases} \quad (19)$$

where i_{cr} equals to γ'/γ_w and represents the critical value determining whether liquefaction occurs or not. The above equation is illustrated in the v_{wz} - i_z space by Fig. 3, which appears clearly as a non-Darcy flow model.

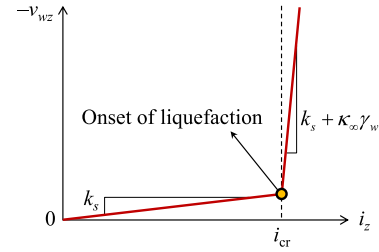


Fig. 3. Schematic of the non-Darcy flow model.

Previous studies also observed the nonlinear v_{wz} - i_z relationships when seepage failure occurs, as shown in Fig. 4. Fukumoto and Ohtsuka (2018) reported a three-dimensional direct particle-fluid simulation model for the seepage failure of granular soils. This model couples DEM and LBM (Lattice Boltzmann Method). The interaction between the soil particles and the seepage flow was also considered. The failure process induced by the seepage flow was captured with no macroscopic assumptions. The obtained evolution of inflow velocity was plotted as a function of the hydraulic gradient, as shown in Fig. 4(a). The piping experiments by Skempton and Brogan (1994) provides another evidence for the nonlinear v_{wz} - i_z relationship during seepage failure, as presented in Fig. 4(b). These evidences indicate that the pore-fluid velocity can increase significantly if liquefaction occurs, which is reproduced by the non-Darcy model, Eq. (19).

Fig. 5 provides an intuitive comparison between the permeability increase and the non-Darcy flow model by using an imaginary test. If the data from real laboratory experiments is used, the following discussion can be also conducted. As shown in Fig. 5(a), when the liquefied state is not taken into account, a linear Darcy model with constant permeability can be obtained by fitting the points under the non-liquefied state. If the liquefied state is considered and the Darcy model with dynamic permeability (denoted by k_d here) is applied, see Fig. 5(b), k_d will be calculated as the slope from the coordinate origin (0,0) to each data point, because $v_{wz} = -k_d i_z$ is adopted. It is assumed that seven data points are measured during liquefaction. Then, seven values of k_d will be obtained, e.g. $k_d/k_s = 1, 2, 3, 4, 5, 6, 7$ in Fig. 5(b). Note that one may obtain more data points (or less) under the liquefaction state in real laboratory experiments. The point number of seven as well as the specific values of k_d are just used here for an instance and does not affect the conceptual comparison.

If all the data points are connected by a continuous curve, then a bi-linear function can be obtained, as shown in Fig. 5(c). According to the primal constraint Eq. (7) in Section 2.2, the hydraulic gradient i_z should not exceed the limit value i_{cr} . Therefore, for the bi-linear curve in Fig. 5(c), the first stage has a slope of 1 (i.e. $v_{wz} = -k_s i_z$) and the second stage has a slope of ∞ . As aforementioned, the non-Darcy model is based on the penalty method, which fulfills the primal constraint in an approximate manner by taking the penalty parameter κ_∞ as large values. In Fig. 5(c), $\kappa_\infty = 10^6 k_s/\gamma_w$ is applied for an instance. It can be found that this value of κ_∞ can reproduce the ideal bi-linear curve with a sufficient accuracy. Section 5 will further examine the influence of different values of κ_∞ on the numerical results as well as the nonlinear convergence. Therefore, as shown in Fig. 5(d), the reported permeability increases during liquefaction can be rearranged in the v_{wz} - i_z space and can then be regarded as the increase of pore-fluid velocity, acting as additional evidences for the non-Darcy model Eq. (19).

3.3. Discretization

A standard finite element partitioning of the domain Ω is considered for spatial discretization. The discrete versions of the spaces $\mathcal{V}_u \times \mathcal{V}_p$ and $\mathcal{V}_\phi \times \mathcal{V}_\psi$ are denoted by $\mathcal{V}_{u,h} \times \mathcal{V}_{p,h}$ and $\mathcal{V}_{\phi,h} \times \mathcal{V}_{\psi,h}$, respectively. The

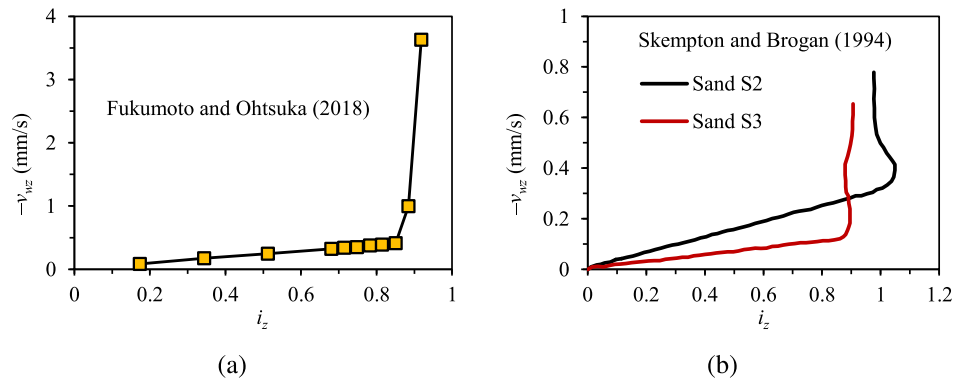


Fig. 4. Evidences for the dual condition: (a) numerical results of non-cohesive granular soils with upward seepage flow (Fukumoto and Ohtsuka, 2018); (b) experimental results on piping in sandy gravels (Skempton and Brogan, 1994).

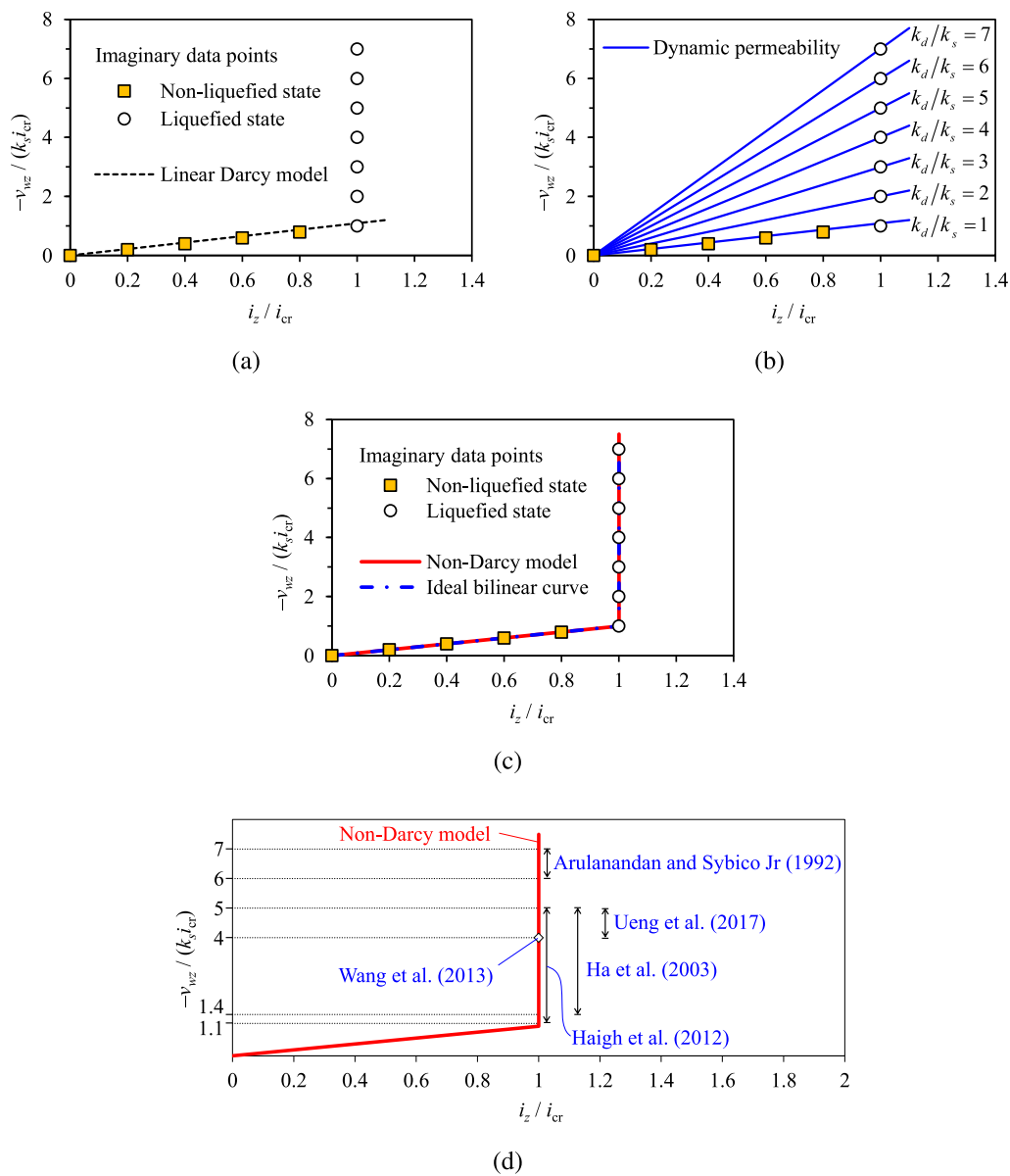


Fig. 5. Conceptual comparison of different models by an imaginary test: (a) conventional Darcy model with constant permeability; (b) Darcy model with dynamic permeability; (c) non-Darcy model; (d) reconsidering permeability increase as non-Darcy flow.

subscript h means the spatially discrete version. Therefore, Eq. (17) is discretized as finding $(\mathbf{u}_h, p_h) \in \mathcal{V}_{u,h} \times \mathcal{V}_{p,h}$ such that there holds:

$$\int_{\Omega} \nabla \Phi_h : (\sigma'_h - p_h \mathbf{I}_{2 \times 2}) \, d\Omega + \int_{\Omega} \Phi_h \cdot \mathbf{b} \, d\Omega + \int_{\Gamma_\sigma} \Phi_h \cdot \hat{\mathbf{t}} \, d\Gamma = 0, \quad (20a)$$

$$\int_{\Omega} \phi_h \left(\frac{\partial \varepsilon_{v,h}}{\partial t} + n\beta \frac{\partial p_h}{\partial t} \right) \, d\Omega - \int_{\Omega} \nabla \phi_h \cdot \mathbf{v}_{w,h} \, d\Omega + \int_{\Gamma_v} \phi_h \hat{v}_w^n \, d\Gamma = 0. \quad (20b)$$

for all $(\Phi_h, \phi_h) \in \mathcal{V}_{\Phi,h} \times \mathcal{V}_{\phi,h}$.

For temporal discretization, the backward Euler method is applied. Applying a time integration to Eq. (20b), the fully discrete variational formulation can be obtained:

$$\int_{\Omega} \nabla \Phi_h : (\sigma'^t_h - p'^t_h \mathbf{I}_{2 \times 2}) \, d\Omega + \int_{\Omega} \Phi_h \cdot \mathbf{b} \, d\Omega + \int_{\Gamma_\sigma} \Phi_h \cdot \hat{\mathbf{t}} \, d\Gamma = 0, \quad (21a)$$

$$\begin{aligned} & \int_{\Omega} \phi_h \left(\varepsilon^t_{v,h} + n\beta p'^t_h \right) \, d\Omega - \tau \int_{\Omega} \nabla \phi_h \cdot \mathbf{v}'_{w,h} \, d\Omega + \tau \int_{\Gamma_v} \phi_h \hat{v}_w^n \, d\Gamma \\ & = \int_{\Omega} \phi_h \left(\varepsilon^{t-\tau}_{v,h} + n\beta p^{t-\tau}_h \right) \, d\Omega. \end{aligned} \quad (21b)$$

where τ denotes the time step.

3.4. Linearization by the Newton–Raphson method

In the present model, the nonlinearity comes from the nonlinear relationship between the pore-fluid velocity \mathbf{v}_w and the hydraulic gradient \mathbf{i} . Applying the Newton–Raphson method to the current discrete velocity $\mathbf{v}_{w,h}^{t,k}$, its linearization can be obtained as follows:

$$\mathbf{v}_{w,h}^{t,k} = \mathbf{v}_{w,h}^{t,k-1} + \mathbf{v}'_w \left(\mathbf{i}_h^{t,k} - \mathbf{i}_h^{t,k-1} \right) = \mathbf{v}_{w,h}^{t,k-1} + \frac{\mathbf{v}'_w}{\gamma_w} \left(\nabla p_h^{t,k} - \nabla p_h^{t,k-1} \right), \quad (22)$$

where the subscripts k and $k-1$ represents the current and previous iterations, respectively. \mathbf{v}'_w denotes the partial derivative of \mathbf{v}_w to \mathbf{i} and can be derived from Eq. (19) as follows:

$$\mathbf{v}'_w = \frac{\partial \mathbf{v}_w}{\partial \mathbf{i}} = \begin{bmatrix} -k_s & 0 \\ 0 & v'_{wz} \end{bmatrix}, \quad v'_{wz} = \frac{\partial v_{wz}}{\partial i_z} = \begin{cases} -k_s, & \text{if } i_z < i_{cr} \\ -k_s - \kappa_\infty \gamma_w, & \text{if } i_z \geq i_{cr}. \end{cases} \quad (23)$$

With the use of Eq. (22), Eq. (21) is linearized as:

$$\begin{aligned} & \int_{\Omega} \nabla \Phi_h : \sigma'^{t,k}_h \, d\Omega - \int_{\Omega} \nabla \Phi_h : p'^{t,k}_h \mathbf{I}_{2 \times 2} \, d\Omega \\ & + \int_{\Omega} \Phi_h \cdot \mathbf{b} \, d\Omega + \int_{\Gamma_\sigma} \Phi_h \cdot \hat{\mathbf{t}} \, d\Gamma = 0, \end{aligned} \quad (24a)$$

$$\begin{aligned} & \int_{\Omega} \phi_h \varepsilon^t_{v,h} \, d\Omega + \int_{\Omega} \phi_h n\beta p'^{t,k}_h \, d\Omega - \tau \int_{\Omega} \nabla \phi_h \cdot \frac{\mathbf{v}'_w}{\gamma_w} \nabla p_h^{t,k} \, d\Omega \\ & + \tau \int_{\Gamma_v} \phi_h \hat{v}_w^n \, d\Gamma = \\ & \int_{\Omega} \phi_h \varepsilon^{t-\tau}_{v,h} \, d\Omega + \int_{\Omega} \phi_h n\beta p^{t-\tau}_h \, d\Omega - \tau \int_{\Omega} \nabla \phi_h \cdot \frac{\mathbf{v}'_w}{\gamma_w} \nabla p_h^{t,k-1} \, d\Omega \\ & + \tau \int_{\Omega} \nabla \phi_h \cdot \mathbf{v}_{w,h}^{t,k-1} \, d\Omega. \end{aligned} \quad (24b)$$

It is apparent that the above non-Darcy formulation is intrinsically different from the dynamic permeability formulation derived in Zhou et al. (2020b). The difference can be compared by the linearized equations, or alternatively, the conceptual comparison in Fig. 5 can be recalled here to provide an intuitive representation. In the non-Darcy model, \mathbf{v}'_w used in Eq. (24) is the tangential slope of the \mathbf{v}_w - \mathbf{i} relationship, as discussed in Fig. 5(c). However, dynamic permeability (k_d) is the secant slope of the \mathbf{v}_w - \mathbf{i} relationship, as shown in Fig. 5(b). It is therefore not surprising that the tangential slope will obtain better convergences, i.e. the non-Darcy model can overcome the convergence difficulties induced by dynamic permeability.

3.5. Algebraic representation

To obtain the algebraic representations for numerical implementation, \mathbf{d}_u and \mathbf{d}_p are used to denote the discrete unknown vectors for the displacement (u) and the excessive pore pressure (p). Their shape function matrices are denoted by \mathbf{N}_u and \mathbf{N}_p , respectively. By employing the standard Galerkin method, \mathbf{N}_u and \mathbf{N}_p are also the weighting function vectors. Eq. (24) can then be rewritten as the following matrix system:

$$\begin{bmatrix} \mathbf{K} & \mathbf{G} \\ \mathbf{G}^T & \mathbf{H} + \mathbf{L} \end{bmatrix} \begin{Bmatrix} \mathbf{d}_u^{t,k} \\ \mathbf{d}_p^{t,k} \end{Bmatrix} = \begin{Bmatrix} \mathbf{F}_u \\ \mathbf{F}_p \end{Bmatrix}, \quad (25)$$

where

$$\begin{aligned} \mathbf{K} &= \int_{\Omega} \mathbf{B}_u^T \mathbf{D} \mathbf{B}_u \, d\Omega, \\ \mathbf{G} &= - \int_{\Omega} \mathbf{B}_u^T \mathbf{m} \mathbf{N}_p \, d\Omega, \\ \mathbf{H} &= - \int_{\Omega} n\beta \mathbf{N}_p^T \mathbf{N}_p \, d\Omega, \\ \mathbf{L} &= \frac{\tau}{\gamma_w} \int_{\Omega} \mathbf{B}_p^T \mathbf{v}'_w \mathbf{B}_p \, d\Omega, \\ \mathbf{F}_u &= - \int_{\Omega} \mathbf{N}_u^T \mathbf{b} \, d\Omega - \int_{\Gamma_\sigma} \mathbf{N}_u^T \hat{\mathbf{t}} \, d\Gamma, \end{aligned} \quad (26)$$

$$\mathbf{F}_p = \mathbf{G}^T \mathbf{d}_u^{t-\tau} + \mathbf{H} \mathbf{d}_p^{t-\tau} + \mathbf{L} \mathbf{d}_p^{t,k-1} + \tau \int_{\Gamma_v} \mathbf{N}_p^T \hat{v}_w^n \, d\Gamma - \tau \int_{\Omega} \mathbf{B}_p^T \mathbf{v}_{w,h}^{t,k-1} \, d\Omega,$$

with

$$\mathbf{B}_u = \nabla \mathbf{N}_u, \quad \mathbf{m} = \{1, 1, 0, 0\}^T, \quad \mathbf{B}_p = \nabla \mathbf{N}_p. \quad (27)$$

Based on the above algebraic representations, one can easily derive the iterative procedure for finding the solution $(\mathbf{d}_u^t, \mathbf{d}_p^t)$, because the Newton–Raphson method is standard in the conventional finite element framework. The present model is implemented in the in-house finite element code (Zhou et al., 2016a,b, 2018; Wang et al., 2019; Zhou et al., 2020a,b, 2021; Yin et al., 2021). It is highlighted here again that the present model does not require coding constrained variational principle and can be therefore conveniently incorporated into other codes, e.g. PORO-FSSI-FOAM (Liang et al., 2020; Liang and Jeng, 2021). This is a main improvement over our previous NCP treatment (Zhou et al., 2021).

4. Cylinder tests under one-dimensional (1D) wave loading

4.1. Computational model

In this section, the present model is used to reproduce the cylinder tests (Liu et al., 2015). The boundary conditions are shown in Fig. 6. On the bottom and both sides of the seabed, the displacement and pore-fluid flow along the normal direction are constrained as zero. At the seabed surface, the pore pressure of the fluid phase is constrained as the wave pressure $P_b = p_0 \cos(2\pi t/T)$, and P_b is also applied as a distributed pressure to the solid phase. The element size along the z direction is taken as 0.12 m. For the temporal discretization, one wave period is divided into 40 time steps.

Liu et al. (2015) reported 24 cylinder tests under 1-D wave loading conditions using a 1.8 m thick sandy deposit, by changing the soil porosity n , soil saturation S_r , wave period T and pressure amplitude p_0 . Twelve of these tests were simulated by Zhou et al. (2020b). It was reported that removing tensile behavior in numerical method provided a better agreement with the experimental results. Zhou et al. (2021) investigated six tests by Liu et al. (2015) and obtained a similar conclusion. It is therefore not necessary to repeat comparing numerical results with that many tests. In this study, two tests (i.e. ‘Test 2’ and ‘Test 20’ Liu et al., 2015) are considered.

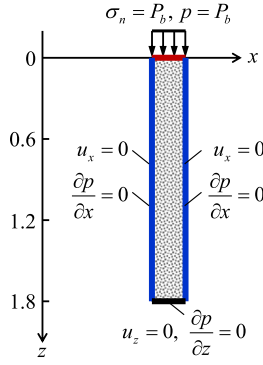
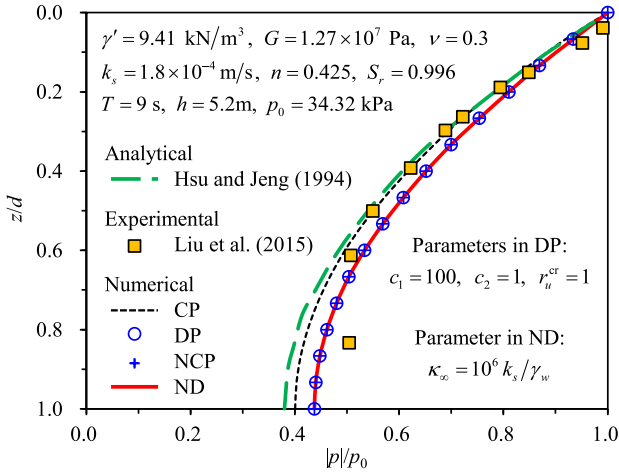


Fig. 6. Boundary conditions of the cylinder tests.

Fig. 7. The pressure amplitude $|p|/p_0$ versus the soil depth z/d of 'Test 20'.

During the simulation, four numerical treatments are investigated: CP (the conventional Darcy model using **Constant Permeability**), DP (**Dynamic Permeability** model Zhou et al., 2020b), NCP (**Nonlinear Complementarity Problem** using the Lagrange multiplier method Zhou et al., 2021) and ND (**non-Darcy** model presented in this study). DP model uses the parameters $c_1 = 100$, $c_2 = 1$ and $r_u^{cr} = 1$, which are recommended by Zhou et al. (2020b). ND model takes the penalty parameter as $\kappa_\infty = 10^6 k_s / \gamma_w$. Note that NCP (Zhou et al., 2021) is a parameter-free treatment.

4.2. Pore pressure and corresponding liquefaction analysis

First, the 'Test 20' (Liu et al., 2015), where liquefaction was observed, is simulated. Fig. 7 gives the vertical distribution of pressure amplitude as well as the computational parameters. CP model is found to achieve a good agreement with the analytical solution (Hsu and Jeng, 1994), validating the in-house code developed in this study. Other three numerical models (DP, NCP and ND) obtain nearly identical results, which also coincide with the experimental data in a reasonable sense. The difference between these four numerical models in the pressure amplitude is not significant, but can become apparent by comparing other results, e.g., Fig. 8.

Fig. 8(a) gives the liquefaction depths determined by the criterion Eq. (4). The liquefaction depths by DP, NCP and ND are almost the same and smaller than that by CP. For a typical instant of 0.425T shown in Fig. 8(a), Fig. 8(b) and Table 1 further provides the vertical effective stress $\gamma'z - (p - P_b)$. The maximum tensile stress by CP model is -1367.30 Pa. This tensile stress is nonphysical in a non-cohesive seabed (Qi and Gao, 2018) and is reduced by DP, NCP and ND to

Table 1

Vertical effective stress at $t = 0.425T$ during the numerical simulation of 'Test 20'.

| z (m) | z/d | $\gamma'z - (p - P_b)$ (Pa) | | | |
|------------------------|-------|-----------------------------|---------|---------|---------|
| | | CP | DP | NCP | ND |
| 0.00 | 0.00 | 0 | 0 | 0 | 0 |
| 0.12 | 0.07 | -596.54 | -7.93 | 0 | -0.0008 |
| 0.24 | 0.13 | -1022.96 | -10.74 | 0 | -0.0014 |
| 0.36 | 0.20 | -1278.54 | -12.59 | 0 | -0.0019 |
| 0.48 | 0.27 | -1367.30 | -8.85 | 0 | -0.0022 |
| 0.60 | 0.33 | -1296.75 | -3.97 | 0 | -0.0023 |
| 0.72 | 0.40 | -1076.81 | 21.79 | 24.98 | 24.97 |
| 0.84 | 0.47 | -718.78 | 206.93 | 209.44 | 209.43 |
| 0.96 | 0.53 | -234.60 | 542.73 | 544.68 | 544.68 |
| 1.08 | 0.60 | 363.83 | 1017.74 | 1019.27 | 1019.27 |
| 1.20 | 0.67 | 1065.25 | 1619.57 | 1620.79 | 1620.79 |
| 1.32 | 0.73 | 1859.42 | 2336.12 | 2337.12 | 2337.12 |
| 1.44 | 0.80 | 2737.55 | 3156.53 | 3157.37 | 3157.37 |
| 1.56 | 0.87 | 3692.52 | 4071.77 | 4072.51 | 4072.51 |
| 1.68 | 0.93 | 4719.11 | 5075.15 | 5075.83 | 5075.83 |
| 1.80 | 1.00 | 5814.12 | 6162.53 | 6163.19 | 6163.19 |
| Liquefaction depth (m) | | 1.007 | 0.618 | 0.600 | 0.600 |

Table 2

Vertical effective stress at $t = 0.45T$ during the numerical simulation of 'Test 2'.

| z (m) | z/d | $\gamma'z - (p - P_b)$ (Pa) | | | |
|------------------------|-------|-----------------------------|---------|---------|---------|
| | | CP | DP | NCP | ND |
| 0.00 | 0.00 | 0 | 0 | 0 | 0 |
| 0.12 | 0.07 | -5212.26 | -93.87 | 0 | -0.0100 |
| 0.24 | 0.13 | -8733.08 | -151.41 | 0 | -0.0185 |
| 0.36 | 0.20 | -10637.49 | -192.80 | 0 | -0.0256 |
| 0.48 | 0.27 | -11240.89 | -199.46 | 0 | -0.0312 |
| 0.60 | 0.33 | -10914.84 | -179.65 | 0 | -0.0353 |
| 0.72 | 0.40 | -9996.78 | -127.28 | 0 | -0.0380 |
| 0.84 | 0.47 | -8751.18 | -43.47 | 0 | -0.0392 |
| 0.96 | 0.53 | -7362.50 | 150.94 | 162.63 | 162.61 |
| 1.08 | 0.60 | -5945.02 | 1136.63 | 1145.28 | 1145.27 |
| 1.20 | 0.67 | -4559.45 | 2463.49 | 2472.71 | 2472.70 |
| 1.32 | 0.73 | -3230.09 | 3873.81 | 3884.12 | 3884.11 |
| 1.44 | 0.80 | -1959.72 | 5254.20 | 5265.26 | 5265.25 |
| 1.56 | 0.87 | -740.78 | 6566.01 | 6577.46 | 6577.45 |
| 1.68 | 0.93 | 436.83 | 7802.55 | 7814.16 | 7814.15 |
| 1.80 | 1.00 | 1580.87 | 8966.55 | 8978.20 | 8978.19 |
| Liquefaction depth (m) | | 1.007 | 0.618 | 0.600 | 0.600 |

-12.59 Pa, 0 and -0.0023 Pa, respectively. From an engineering point of view, the error by ND is negligible. If higher accuracy is required, larger penalty parameter κ_∞ is suggested. Note that large parameters in DP will lead to numerical instability (Zhou et al., 2020b). Therefore, only NCP and ND are promising.

Then, the 'Test 2' (Liu et al., 2015), where the saturation degree S_r equals to 0.951, is simulated. The only difference from 'Test 20' ($S_r = 0.996$) is the saturation. As illustrated in Fig. 9, the results by DP, NCP and ND are still close to each other. The liquefaction depth by CP is overestimated, because abnormally large tensile stress occurs. As shown in Table 2, the maximum tensile stress by CP reaches to -11 240.89 Pa, which is reduced by DP, NCP and ND to -199.46 Pa, 0 and -0.0392 Pa, respectively. Although the tensile value (-0.0392 Pa) by ND here in 'Test 2' is larger than that in 'Test 20' (-0.0023 Pa), it is still close to zero and hence can be also neglected.

4.3. Hydraulic gradient and corresponding liquefaction analysis

The above liquefaction analysis is conducted based on using the criterion Eq. (4). In this subsection, another criterion Eq. (5) is investigated and compared with Eq. (4). Considering that Eq. (5) is given in terms of the hydraulic gradient, a finer mesh with z -directional

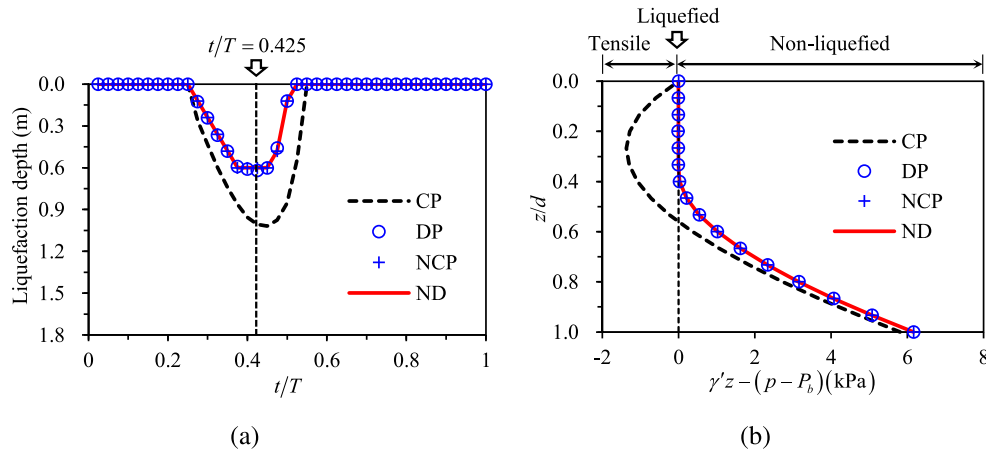


Fig. 8. Liquefaction analysis of 'Test 20' by the criterion Eq. (4): (a) temporal liquefaction depth; and (b) vertical distribution of $\gamma'z - (p - P_b)$ at the instant of $0.425T$.

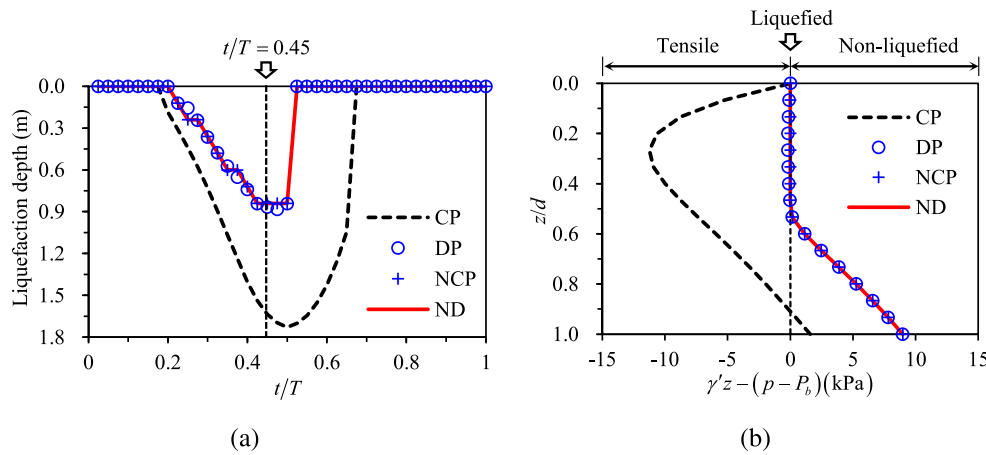


Fig. 9. Liquefaction analysis of 'Test 2' by the criterion Eq. (4): (a) temporal liquefaction depth; and (b) vertical distribution of $\gamma'z - (p - P_b)$ at the instant of $0.45T$.

element size of 0.01 m is used here to guarantee the accuracy. With this mesh, DP and NCP models are not considered, due to the following two considerations. First, DP model was found to cause numerical instability in this fine mesh, as demonstrated in Section 4.4. Second, the above results have clearly shown that the difference between ND and NCP is not significant. Therefore, only CP and ND models are discussed in this subsection.

As presented in Fig. 10(a), if CP model is used, Eq. (5) obtains apparently smaller liquefaction depth than Eq. (4). In contrast, when ND model is used, the liquefaction depths determined by the two criteria become unified. For the instant of $0.425T$, Fig. 10(b) provides the vertical distributions of $\gamma'z - (p - P_b)$ and $\gamma' - j_z$, where the negative values mean the tensile stresses induced in the volumetric soil element or across the surface of the vertical soil column. This nonphysical behavior is nearly removed by ND model. Fig. 11 shows the numerical results of 'Test 2'. For seabed under lower saturation, CP model leads to larger discrepancy between the two criteria which are unified again by ND model presented in this study.

4.4. Nonlinear convergence performances

Among the four numerical treatments, CP model is linear. Hence, the non-linear convergence performances of the other three models, i.e. DP, NCP and ND, are discussed in this subsection by simulating 'Test 2' (Liu et al., 2015). Fig. 12 shows the iteration numbers cost by each time step by using the coarser mesh in Section 4.2 and the finer mesh in Section 4.3, whose z -directional element sizes are 0.12 m and 0.01

m, respectively. The liquefaction depth is provided in this figure as a reference. With the use of coarser mesh, NCP and ND both require only 2–5 iterations to achieve the convergence, while DP poses apparently more iterations. The performance of DP model is even worse by using the finer mesh, when the algorithm diverges at the instant of $0.4T$. For the finer mesh, NCP takes a little more iterations than ND, because ND is treated by Newton–Raphson method and NCP is handled by PDASS, which is not as smooth as Newton–Raphson method.

4.5. Parametric study on the instantaneous liquefaction depth

According to the above discussions, CP model generally leads to tensile stresses in the liquefied zone. To improve the prediction accuracy, a concise suggestion is presented for the engineering applications as below. First, CP model is used to determine whether there is liquefaction or not. If there is no liquefaction, ND model will provide identical results with CP model and therefore is not needed. If liquefaction occurs, then ND model is required to remove the unreasonable tensile stresses. In this subsection, the effects of ND model on the liquefaction depths are investigated by conducting a parametric study.

During the parametric study, the computational model of the cylinder test shown in Fig. 6 is adopted and a benchmark test is set. The computational parameters of the benchmark test are listed in Table 3. Four soil parameters (Young's modulus E , permeability coefficient k_s , saturation degree S_r and soil porosity n) and three wave parameters (wave period T , water depth h and wave height H) are tested. The seabed thickness d is also tested. Note that the buoyant unit weight γ'

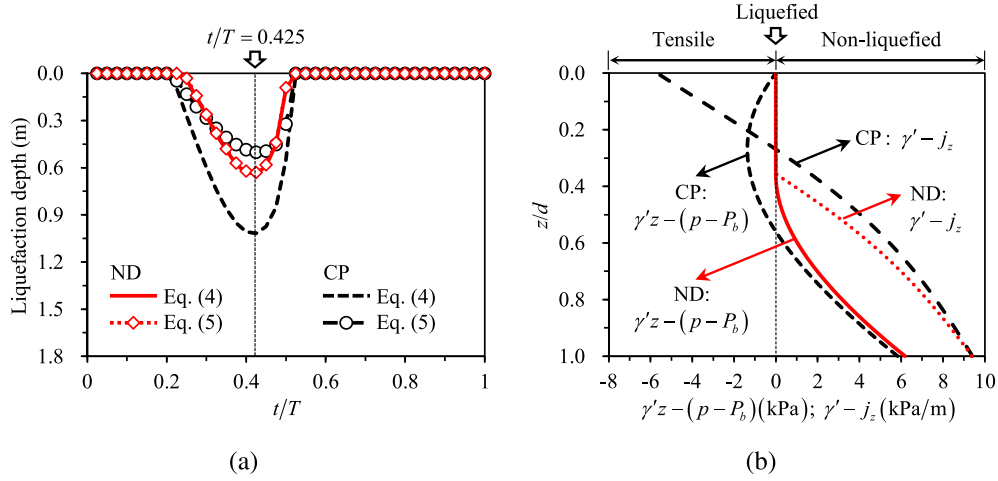


Fig. 10. Liquefaction analysis of 'Test 20' by the criteria Eqs. (4) and (5): (a) temporal liquefaction depth; and (b) vertical distributions of $\gamma'z - (p - P_b)$ and $\gamma' - j_z$ at the instant of $0.425T$.

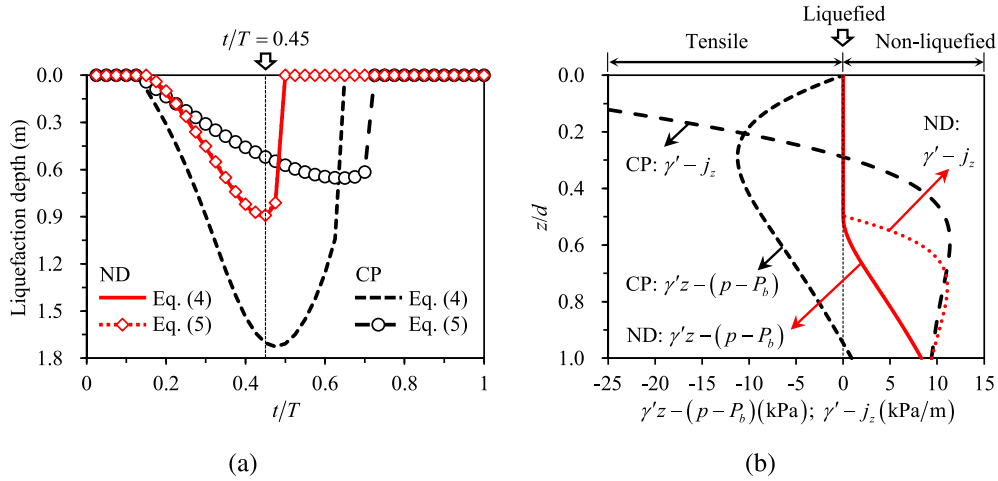


Fig. 11. Liquefaction analysis of 'Test 2' by the criteria Eqs. (4) and (5): (a) temporal liquefaction depth; and (b) vertical distribution of $\gamma'z - (p - P_b)$ and $\gamma' - j_z$ at the instant of $0.45T$.

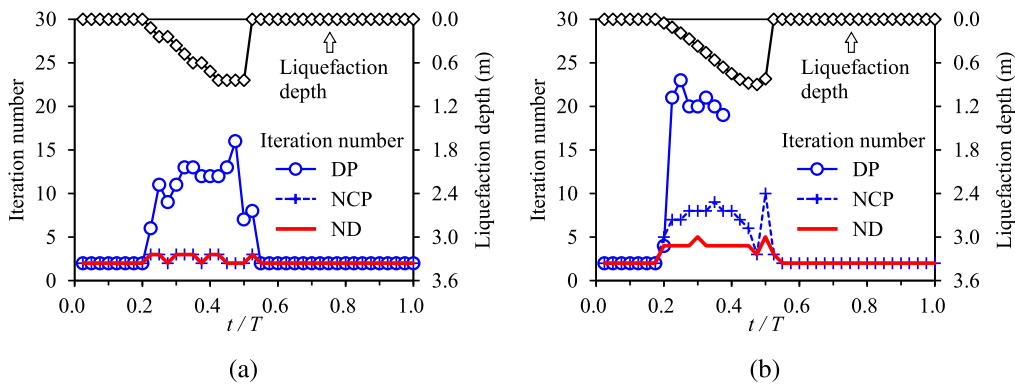


Fig. 12. Iteration number and liquefaction depth versus time step during the numerical simulation of 'Test 2' by using: (a) coarser mesh; and (b) finer mesh.

changes with n and is determined by: $\gamma' = (G_s - 1)(1 - n)\gamma_w$, with G_s given as 2.67 in this paper. In the benchmark test, γ' equals to 9.41 kN/m^3 and the Poisson's ratio ν is taken as 0.3. It is also notable that the wave parameters herein may be beyond the linear wave theory. The influence of wave non-linearity will be included in our future works.

Considering that the criterion by Eq. (4) is the most widely applied one for seabed liquefaction, this section uses Eq. (4) to determine the liquefaction depths for both CP and ND models. As shown in Fig. 13, the liquefaction depth increases with the increase of E , n , T and H but decreases with the increase of k_s , S_r and h . These tendencies

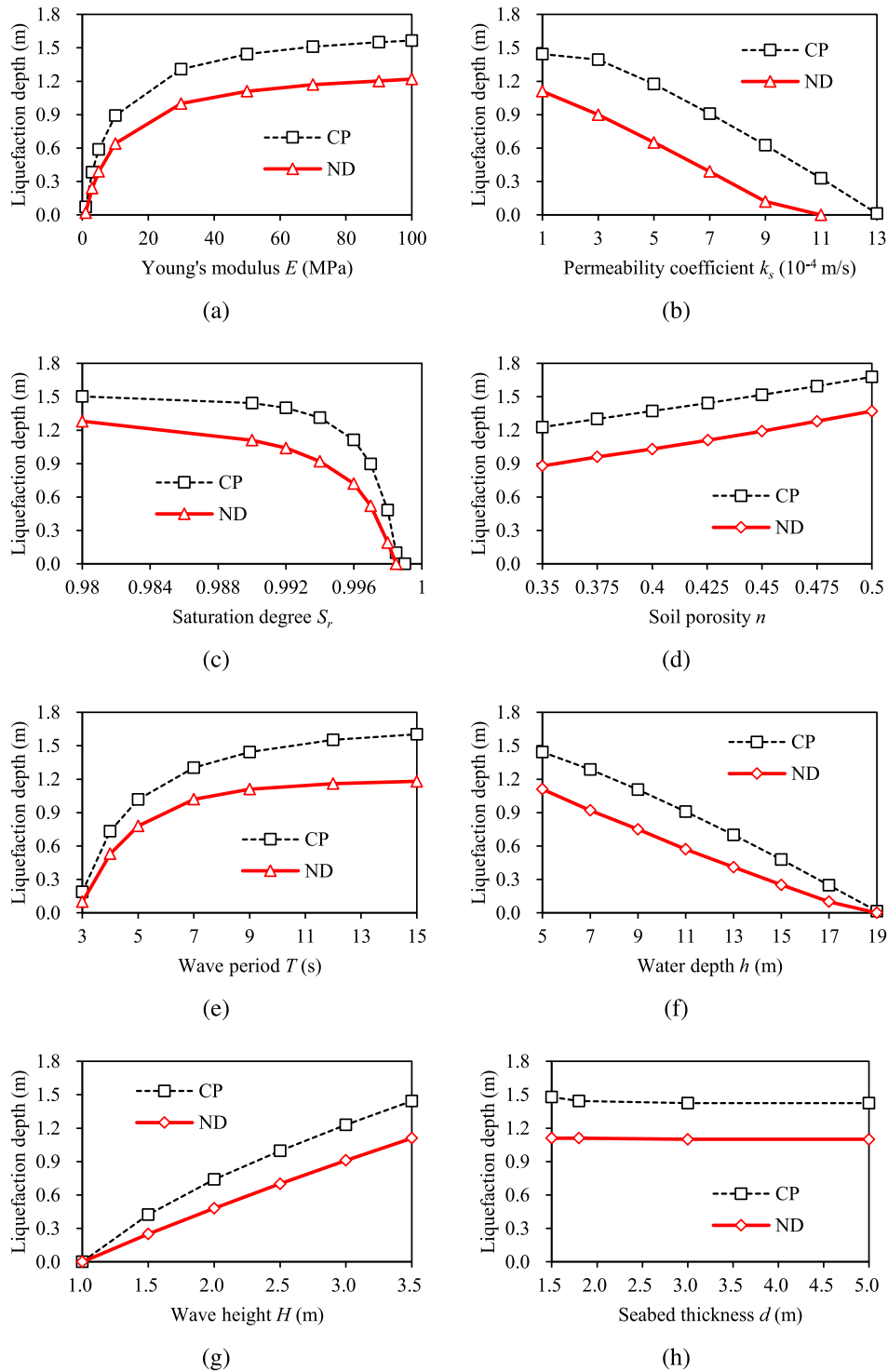


Fig. 13. Liquefaction depths versus (a) Young's modulus E ; (b) permeability coefficient k_s ; (c) saturation degree S_r ; (d) soil porosity n ; (e) wave period T ; (f) water depth h ; (g) wave height H ; (h) seabed thickness d .

Table 3

The computational parameter of the benchmark test in the parametric study.

| Parameter | E (MPa) | k_s (m/s) | S_r (-) | n (-) | T (s) | h (m) | H (m) | d (m) |
|-----------|-----------|--------------------|-----------|---------|---------|---------|---------|---------|
| Value | 50 | 1×10^{-4} | 0.99 | 0.425 | 9 | 5 | 3.5 | 1.8 |

are well corroborated by the general characteristics of wave-seabed interactions (Jeng, 2018). Moreover, when the liquefaction depth is

larger, the difference between the CP and ND models becomes more apparent. It is notable that the influence of seabed thickness d on the liquefaction depth is insignificant in the parametric study presented here but can become significant under some 2D wave conditions (Jeng, 2018).

The liquefaction depths predicted by the two models are then plotted in Fig. 14, wherein all the results of Fig. 13 are collected together. In Fig. 14, the abscissa z_{CP} denotes the liquefaction depth by CP model. The ordinate z_{ND} denotes the liquefaction depth by ND model. A

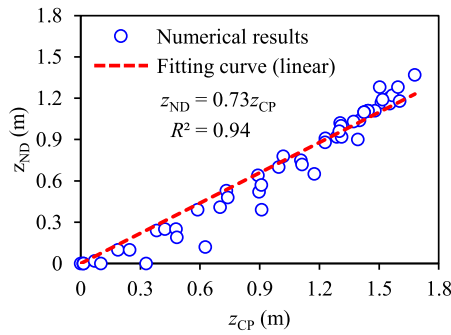


Fig. 14. Relationship of the liquefaction depths by CP and ND models.

linear relationship is found to fit well with the numerical results. The correlation coefficient is $R^2 = 0.94$. The instantaneous liquefaction depth by ND model is roughly 0.73 times the value by CP model. This relationship can be used as a quick reference for engineering practice because the analytical solution for CP model is available in the literature (Hsu and Jeng, 1994) and commonly used in offshore geotechnical engineering industry. It should be noted that this quick

estimation is obtained herein for a sandy seabed in shallow marine settings under the assumption of linear waves. If more general scenarios need to be considered, systematical studies are required to include more factors, or alternatively, one can use our non-Darcy model to conduct numerical simulations for specific applications.

5. Two-dimensional (2D) wave-seabed interactions

5.1. Computational model and parameters

This section applies the present non-Darcy flow model to analyze the 2D wave-seabed interactions. Fig. 15 shows the adopted computational mesh. Due to that there is no structure here, the liquefaction analysis will focus on the shallow layer. Therefore, smaller element sizes are used in the relevant regions. The computational parameters are given in Fig. 15, which are the same to those in ‘Test 2’ (Liu et al., 2015). The penalty parameter in ND model is taken as $\kappa_\infty = 10^6 k_s / \gamma_w$. CP, DP and NCP models are used in the simulation for comparative study. The DP parameters ($c_1 = 10$, $c_2 = 1$, $r_u^{cf} = 1$) used in 2D simulation by Zhou et al. (2020b) are also applied here in the DP model. NCP model needs no additional parameters.

The seabed thickness is taken as 100 m, which is larger than the wavelength ($L \approx 61.4$ m here). This setup can be used to simulate

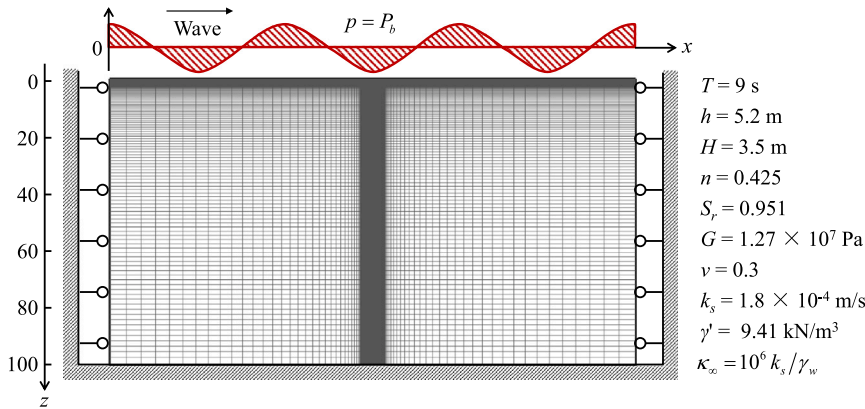


Fig. 15. Computational mesh, parameters and boundary conditions used in the 2D pure-seabed simulation.

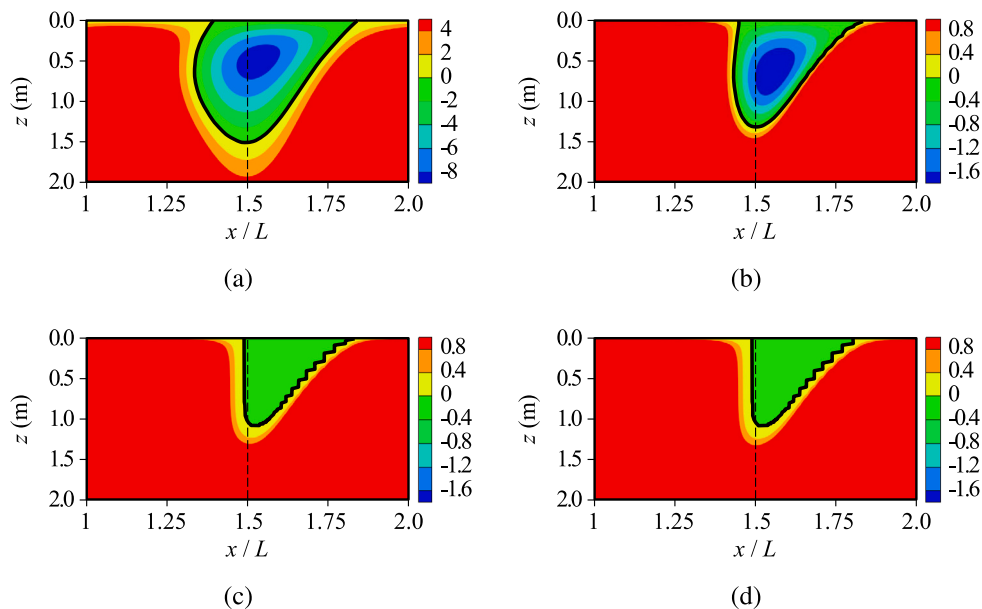


Fig. 16. The vertical effective stress $\gamma'z - (p - P_b)$ (kPa) by: (a) CP; (b) DP with parameters of $c_1 = 10$, $c_2 = 1$ and $r_u^{cf} = 1$; (c) NCP; (d) ND with penalty parameter of $\kappa_\infty = 10^6 k_s / \gamma_w$.

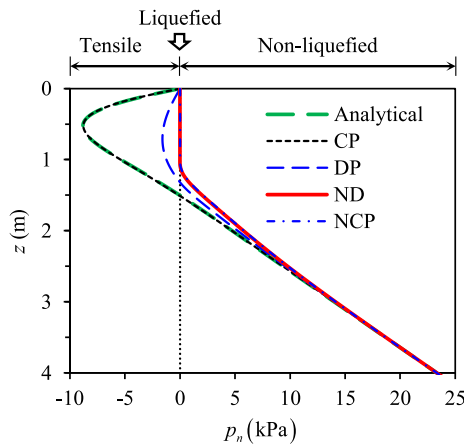


Fig. 17. Vertical distribution of the vertical effective stress $\gamma'z - (p - P_b)$ along the line of $x = 1.5L$. Note: the analytical solution: Yamamoto et al. (1978).

a seabed with infinite thickness (Yamamoto et al., 1978; Hsu et al., 1993). The seabed length is set as three times of the wavelength L (Ye and Jeng, 2012) to minimize the influence of the x -directional boundary and meanwhile minimize the computational effort. Fig. 15 also illustrates the boundary conditions, which are similar to those given in Fig. 6. The only difference is that the wave pressure P_b here is a function of both x -axis and time t , as given by Eq. (1).

5.2. Numerical results

The liquefaction analysis focuses on a region around $x = 1.5L$, where the wave trough arrives at $t = T$. Therefore, the numerical results are given at the instant of $t = T$. Fig. 16 presents the contours of the vertical effective stress $\gamma'z - (p - P_b)$ obtained by four models. Their vertical distributions along the line of $x = 1.5L$ are given by Fig. 17, wherein the results by CP model agrees exactly with the analytical solution (Yamamoto et al., 1978). This again validates the numerical code.

As shown in Figs. 16 and 17, the tensile behavior by CP model is considerable. It is eased by DP model but still non-negligible. Larger values of c_1 are expected theoretically to further reduce the tensile behavior. Unfortunately, the numerical algorithm may diverge when using large c_1 (Zhou et al., 2020b). In contrast, both NCP and ND models are free of nonphysical tensile phenomenon as well as numerical instability. Noting that large penalty parameter κ_∞ in ND model is the key to remove the tensile behavior, the nonlinear performance becomes another important concern, as addressed in the next subsection.

By finding the isoline of $\gamma'z - (p - P_b) = 0$ (i.e. the black lines in Fig. 16), the liquefied zones can be determined by Eq. (4) and are further compared in Fig. 18. NCP and ND models are found to obtain nearly the same results and can be referred to the accurate estimation. Hence, the comparison indicates that CP model overestimates the liquefaction potential. The liquefaction estimation by DP can be regarded as an intermediate result from CP towards the accurate one, due to that the parameter c_1 is not large enough. A close view of the liquefied zone shows that non-smoothness occurs in both NCP and ND models. This issue was discussed in Zhou et al. (2021) and can be addressed to some extent by using finer computational meshes.

5.3. Effects of the penalty parameter on the results and non-linear convergences

Although the DP and ND models both introduce additional parameters, the difference is that the penalty parameter κ_∞ used in ND model can be taken as large enough and meanwhile do not destroy the

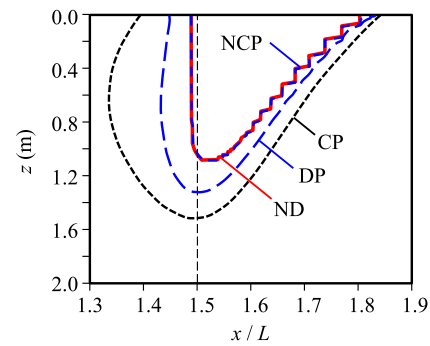


Fig. 18. The liquefied zones determined by Eq. (4) in the 2-D simulation.

numerical algorithm. To validate this performance, four values of κ_∞ are tested, i.e. 10 , 10^2 , 10^4 and 10^6 times of k_s/γ_w . The results by using $\kappa_\infty = 10^6 k_s/\gamma_w$ have been discussed in the above subsection and are compared here with the other three cases by Fig. 19(a) in the vertical effective stress $\gamma'z - (p - P_b)$ and by Fig. 19(b) in the liquefied zone. In these two comparisons, the results by CP model are provided as a reference.

As shown in Fig. 19(a), if the penalty parameter κ_∞ is not large enough (e.g. $\kappa_\infty = 10 k_s/\gamma_w$ or $10^2 k_s/\gamma_w$), the tensile stresses cannot be removed. For the case of $\kappa_\infty = 10 k_s/\gamma_w$, the tensile stresses are still apparent despite the apparent improvement over CP model. The value of $\kappa_\infty = 10^2 k_s/\gamma_w$ can make the tensile stresses at a much lower value but still not close to zero. The residuals of tensile stresses have a significant influence on the liquefaction zones shown in Fig. 19(b). In contrast, large penalty parameters (e.g., $\kappa_\infty = 10^4 k_s/\gamma_w$ and $10^6 k_s/\gamma_w$) provide a satisfactory accuracy in removing the tensile stresses. The results by these two values are almost the same. This implies that the increase of κ_∞ will achieve a converged result, making ND model somehow a parameter-free treatment. More precisely, once κ_∞ is large enough (e.g., $10^4 k_s/\gamma_w$), the further variation of κ_∞ will have a negligible influence on the numerical results. The above performance is a common consequence of the penalty method within the constrained variational principle. In this study, the value of $\kappa_\infty = 10^6 k_s/\gamma_w$ is used as a conservative choice.

Then, the effects of the penalty parameter on the nonlinear convergence performance are studied by examining the iteration number cost by each time step, as shown in Fig. 20(a). It is found that ND model requires not more than 12 iterations to deal with the non-linearity. The value of $\kappa_\infty = 10 k_s/\gamma_w$ costs fewer iterations than the other three penalty parameters, but the difference is not significant. For the value of $\kappa_\infty = 10^6 k_s/\gamma_w$, the convergence is further compared with DP and NCP models in Fig. 20(b). DP model requires apparently more iterations than NCP and ND models even a relatively small value of c_1 (i.e., 10) is used in DP, noting that large values of c_1 in DP lead to algorithm divergence (Zhou et al., 2020b). ND obtains faster non-linear convergence than NCP (handled by PDASS), due to the use of Newton–Raphson method.

The above comparisons indicate that the penalty parameter can be chosen large enough to guarantee the numerical accuracy, and generally there is no need to worry about the nonlinear convergence as well as the computational efficiency.

6. Conclusions

In this study, a non-Darcy flow model is proposed to deal with the instantaneous liquefaction in a non-cohesive seabed. Based on numerical examples presented, the following conclusions can be drawn.

(1) Compared with the Darcy model with constant permeability, the present model reproduces the pore-fluid velocity increase during

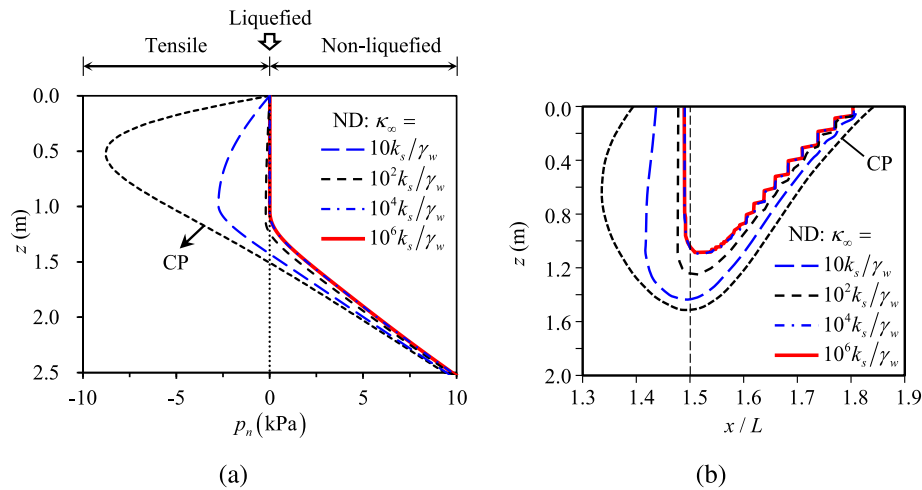


Fig. 19. Parametric study of the penalty parameter κ_∞ : (a) vertical distribution of the vertical effective stress $\gamma'z - (p - P_b)$ along the line of $x = 1.5L$; (b) liquefied zones determined by Eq. (4).

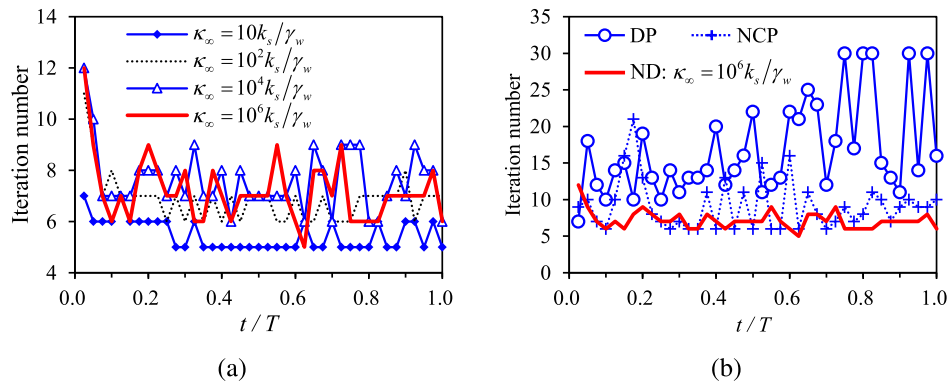


Fig. 20. Iteration number versus time step by: (a) different penalty parameters in ND model; and (b) different models.

liquefaction as well as eliminates the fallacious tensile behavior in a non-cohesive seabed. Moreover, two instantaneous liquefaction criteria widely applied in ocean engineering are unified by the present model. According to the parametric study, the liquefaction depth by the present model is found to be roughly 0.73 times of the value predicted by constant permeability.

(2) Compared with the dynamic permeability model (Zhou et al., 2020b), the present model overcomes the difficulties in the nonlinearity treatment and achieves superior convergences. The penalty parameter introduced by the present model is found to have slight influence on the nonlinear convergence, indicating that the additional computational efforts of using larger penalty values are negligible in spite of their stronger non-linearities. Therefore, the penalty parameter can be chosen large enough so that the tensile behavior can be sufficiently eliminated.

(3) Compared with the non-linear complementarity problem using Lagrange multiplier method (Zhou et al., 2021), the present model obtained nearly identical numerical results but can be easily implemented within the standard finite element framework. It is therefore convenient for future works to incorporate the new model into existing codes (e.g. PORO-FSSI-FOAM, Liang et al. (2020) and Liang and Jeng (2021)) for wave-structure-seabed interactions to simulate more complex scenarios with offshore structures.

CRedit authorship contribution statement

Mo-Zhen Zhou: Methodology, Software, Validation, Writing — Original Draft, Visualization. **Wen-Gang Qi:** Conceptualization,

Methodology, Writing — review & editing. **Dong-Sheng Jeng:** Conceptualization, Supervision, Writing — review & editing. **Fu-Ping Gao:** Conceptualization, Supervision, Writing — review & editing.

Declaration of competing interest

The authors declare that they have no known competing financial interests or personal relationships that could have appeared to influence the work reported in this paper.

Acknowledgments

This work was supported by the Fundamental Research Funds for the Central Universities, China (grant number 2021JBM034); and the National Natural Science Foundation of China (grant numbers 11825205, 51808034, 11972036).

References

- Arulanandan, K., Sybico, Jr., J., 1992. Post-liquefaction settlement of sand. In: *The Wroth Memorial Symposium*. pp. 94–110.
- Bear, J., 1972. *Dynamics of Fluids in Porous Media*. Elsevier Scientific Publishing Company, New York.
- Biot, M.A., 1941. General theory of three-dimensional consolidation. *J. Appl. Phys.* 26, 155–164.
- Celli, D., Li, Y., Ong, M.C., Di Risio, M., 2019. The role of submerged berms on the momentary liquefaction around conventional rubble mound breakwaters. *Appl. Ocean Res.* 85, 1–11. <http://dx.doi.org/10.1016/j.apor.2019.01.023>.

- Chang, K.T., Jeng, D.S., 2014. Numerical study for wave-induced seabed response around offshore wind turbine foundation in Donghai offshore wind farm, Shanghai, China. *Ocean Eng.* 85, 32–43.
- Chen, W., Liu, C., He, R., Chen, G., Jeng, D., Duan, L., 2021. Stability of the foundation trench of the immersed tunnel subjected to combined wave and current loading. *Appl. Ocean Res.* 110, 102627. <http://dx.doi.org/10.1016/j.apor.2021.102627>.
- Cuellar, P., Mira, P., Pastor, M., Fernandez Merodo, J.A., Baessler, M., Ruecker, W., 2014. A numerical model for the transient analysis of offshore foundations under cyclic loading. *Comput. Geotech.* 59, 75–86. <http://dx.doi.org/10.1016/j.compgeo.2014.02.005>.
- Dean, R., Dalrymple, R.A., 1984. *Water Wave Mechanics for Engineers and Scientists*. World Scientific.
- Du, X., Sun, Y., Song, Y., Zhu, C., 2021. In-situ observation of wave-induced pore water pressure in seabed silt in the Yellow River Estuary of China. *J. Mar. Environ. Eng.* 10, 305–317.
- Duan, L., Liao, C., Jeng, D.S., Chen, L., 2017. 2D numerical study of wave and current-induced oscillatory non-cohesive soil liquefaction around a partially buried pipeline in a trench. *Ocean Eng.* 135, 39–51. <http://dx.doi.org/10.1016/j.oceaneng.2017.02.036>.
- Elsafiti, H., Oumeraci, H., 2016. A numerical hydro-geotechnical model for marine gravity structures. *Comput. Geotech.* 79, 105–129. <http://dx.doi.org/10.1016/j.compgeo.2016.05.025>.
- Fukumoto, Y., Ohtsuka, S., 2018. 3-D direct numerical model for failure of non-cohesive granular soils with upward seepage flow. *Comput. Part. Mech.* 5, 443–454. <http://dx.doi.org/10.1007/s40571-017-0180-5>.
- Gao, F., Jeng, D., Sekiguchi, H., 2003. Numerical study on the interaction between non-linear wave, buried pipeline and non-homogenous porous seabed. *Comput. Geotech.* 30, 535–547. [http://dx.doi.org/10.1016/S0266-352X\(03\)00053-3](http://dx.doi.org/10.1016/S0266-352X(03)00053-3).
- Girault, V., Wheeler, M., 2008. Numerical discretization of a Darcy-Forchheimer model. *Numer. Math.* 110, 161–198. <http://dx.doi.org/10.1007/s00211-008-0157-7>.
- Ha, I., Park, Y., Kim, M., 2003. Dissipation pattern of excess pore pressure after liquefaction in saturated sand deposits. In: *Geology and Properties of Earth Materials 2003: Soils, Geology, and Foundations*. pp. 59–67.
- Haigh, S.K., Eadington, J., Madabhushi, S.P.G., 2012. Permeability and stiffness of sands at very low effective stresses. *Géotechnique* 62, 69–75. <http://dx.doi.org/10.1680/geot.10.P.035>.
- Han, S., Jeng, D.S., Tsai, C.C., 2019. Response of a porous seabed around an immersed tunnel under wave loading: Meshfree model. *J. Mar. Sci. Eng.* 7, 369. <http://dx.doi.org/10.3390/jmse7100369>.
- Hansbo, S., 2001. Consolidation equation valid for both Darcian and non-Darcian flow. *Géotechnique* 51, 51–54. <http://dx.doi.org/10.1680/geot.2001.51.1.51>.
- Hsu, J., Jeng, D.S., 1994. Wave-induced soil response in an unsaturated anisotropic seabed of finite thickness. *Int. J. Numer. Anal. Methods Geomech.* 18, 785–807. <http://dx.doi.org/10.1002/nag.1610181104>.
- Hsu, J., Jeng, D.S., Tsai, C., 1993. Short-crested wave-induced soil response in a porous seabed of infinite thickness. *Int. J. Numer. Anal. Methods Geomech.* 17, 553–576. <http://dx.doi.org/10.1002/nag.1610170803>.
- Jeng, D.S., 1997. Wave-induced seabed instability in front of a breakwater. *Ocean Eng.* 24, 887–917. [http://dx.doi.org/10.1016/S0029-8018\(96\)00046-7](http://dx.doi.org/10.1016/S0029-8018(96)00046-7).
- Jeng, D.S., 2003. Wave-induced sea floor dynamics. *Appl. Mech. Rev.* 56, 407–429. <http://dx.doi.org/10.1115/1.1577359>.
- Jeng, D.S., 2018. *Mechanics of Wave-Seabed-Structure Interactions: Modelling, Processes and Applications*. Cambridge University Press, <http://dx.doi.org/10.1017/9781316672266>.
- Jeng, D.S., Lin, Y., 1999. Wave-induced pore pressure around a buried pipeline in gibson soil: finite element analysis. *Int. J. Numer. Anal. Methods Geomech.* 23, 1559–1578. [http://dx.doi.org/10.1002/\(SICI\)1096-9853\(199911\)23:13<1559::AID-NAG57>3.0.CO;2-U](http://dx.doi.org/10.1002/(SICI)1096-9853(199911)23:13<1559::AID-NAG57>3.0.CO;2-U).
- Jeng, D.S., Ou, J., 2010. 3D models for wave-induced pore pressures near breakwater heads. *Acta Mech.* 215, 85–104. <http://dx.doi.org/10.1007/200707-010-0303-z>.
- Jeng, D.S., Ye, J.H., Zhang, J.S., Liu, P.F., 2013. An integrated model for the wave-induced seabed response around marine structures: Model verifications and applications. *Coast. Eng.* 72, 1–19.
- Jia, Y., Zhang, L., Zheng, J.X., Jeng, D.S., Shan, H.X., 2014. Effects of wave-induced seabed liquefaction on sediment re-suspension in the Yellow River Delta. *Ocean Eng.* 89, 146–156. <http://dx.doi.org/10.1016/j.oceaneng.2014.08.004>.
- Kudella, M., Oumeraci, H., de Groot, M., Meijers, P., 2006. Large-scale experiments on pore pressure generation underneath a caisson breakwater. *J. Waterw. Port Coast. Ocean Eng. ASCE* 132, 310–324. [http://dx.doi.org/10.1061/\(ASCE\)0733-950X\(2006\)132:4\(310\)](http://dx.doi.org/10.1061/(ASCE)0733-950X(2006)132:4(310)).
- Kunisch, K., Rößch, A., 2002. Primal–dual active set strategy for a general class of constrained optimal control problems. *SIAM J. Optim.* 13, 321–334. <http://dx.doi.org/10.1137/S1052623499358008>.
- Li, K., Guo, Z., Wang, L., Jiang, H., 2019. Effect of seepage flow on shields number around a fixed and sagging pipeline. *Ocean Eng.* 172, 487–500. <http://dx.doi.org/10.1016/j.oceaneng.2018.12.033>.
- Li, Y., Ong, M.C., Tang, T., 2018. Numerical analysis of wave-induced poro-elastic seabed response around a hexagonal gravity-based offshore foundation. *Coast. Eng.* 136, 81–95. <http://dx.doi.org/10.1016/j.coastaleng.2018.02.005>.
- Liang, Z.D., Jeng, D.S., 2021. PORO-FSSI-FOAM Model for seafloor liquefaction around a pipeline under combined random wave and current loading. *Appl. Ocean Res.* 107, 102497. <http://dx.doi.org/10.1016/j.apor.2020.102497>.
- Liang, Z., Jeng, D.S., Liu, J., 2020. Combined wave–current induced seabed liquefaction around buried pipelines: Design of a trench layer. *Ocean Eng.* 212, 107764. <http://dx.doi.org/10.1016/j.oceaneng.2020.107764>.
- Liao, C.C., Chen, J.J., Zhang, Y.Z., 2019. Accumulation of pore water pressure in a homogeneous sandy seabed around a rocking mono-pile subjected to wave loads. *Ocean Eng.* 173, 810–823. <http://dx.doi.org/10.1016/j.oceaneng.2018.12.072>.
- Lin, Z., Guo, Y., Jeng, D.S., Liao, C., Rey, N., 2016. An integrated numerical model for wave–soil–pipeline interactions. *Coast. Eng.* 108, 25–35.
- Lin, Z., Pokrajac, D., Guo, Y., Jeng, D.S., Tang, T., Rey, N., Zheng, J., Zhang, J., 2017. Investigation of nonlinear wave-induced seabed response around mono-pile foundation. *Coast. Eng.* 121, 197–211. <http://dx.doi.org/10.1016/j.coastaleng.2017.01.002>.
- Liu, B., Jeng, D.S., Ye, G., Yang, B., 2015. Laboratory study for pore pressures in sandy deposit under wave loading. *Ocean Eng.* 106, 207–219. <http://dx.doi.org/10.1016/j.oceaneng.2015.06.029>.
- Madsen, O.S., 1978. Wave-induced pore pressures and effective stresses in a porous bed. *Géotechnique* 28, 377–393. <http://dx.doi.org/10.1680/geot.1978.28.4.377>.
- Martin, E., Thornton, C., Utili, S., 2020. Micromechanical investigation of liquefaction of granular media by cyclic 3D DEM tests. *Géotechnique* 70, 906–915. <http://dx.doi.org/10.1680/jgeot.18.P.267>.
- Meng, K., Yang, X., 2010. Optimality conditions via exact penalty functions. *SIAM J. Optim.* 20, 3208–3231. <http://dx.doi.org/10.1137/090771016>.
- Miyamoto, J., Sassa, S., Sekiguchi, H., 2004. Progressive solidification of a liquefied sand layer during continued wave loading. *Géotechnique* 54, 617–629. <http://dx.doi.org/10.1680/geot.54.10.617.56343>.
- Mory, M., Michallet, H., Bonjean, D., Piedra-Cueva, I., Barboud, J.M.P.F., Abadie, S., Breul, P., 2007. A field study of momentary liquefaction caused by waves around coastal structure. *J. Waterw. Port Coast. Ocean Eng. ASCE* 133, 28–38.
- Narsilio, G., Buzzi, O., Fityus, S., Yun, T., Smith, D., 2009. Upscaling of Navier–Stokes equations in porous media: Theoretical, numerical and experimental approach. *Comput. Geotech.* 36, 1200–1206. <http://dx.doi.org/10.1016/j.compgeo.2009.05.006>.
- Popp, A., Seitz, A., Gee, M., Wall, W., 2013. Improved robustness and consistency of 3D contact algorithms based on a dual mortar approach. *Comput. Methods Appl. Mech. Engrg.* 264, 67–80.
- Qi, W.G., Gao, F.P., 2014. Physical modelling of local scour development around a large-diameter monopile in combined waves and current. *Coast. Eng.* 83, 72–81. <http://dx.doi.org/10.1016/j.coastaleng.2013.10.007>.
- Qi, W.G., Gao, F.P., 2015. A modified criterion for wave-induced momentary liquefaction of sandy seabed. *Theor. Appl. Mech. Lett.* 5, 20–23.
- Qi, W.G., Gao, F.P., 2018. Wave induced instantaneously-liquefied soil depth in a non-cohesive seabed. *Ocean Eng.* 153, 412–423. <http://dx.doi.org/10.1016/j.oceaneng.2018.01.107>.
- Qi, W.G., Shi, Y.M., Gao, F.P., 2020. Uplift soil resistance to a shallowly-buried pipeline in the sandy seabed under waves: Poro-elastoplastic modeling. *Appl. Ocean Res.* 95, 102024. <http://dx.doi.org/10.1016/j.apor.2019.102024>.
- Sassa, S., Sekiguchi, H., 2001. Analysis of wave-induced liquefaction of sand beds. *Géotechnique* 51, 115–126.
- Scholtès, L., Chareyre, B., Michallet, H., Catalano, E., Marzougui, D., 2014. Modeling wave-induced pore pressure and effective stress in a granular seabed. *Contin. Mech. Thermodyn.* 27, 305–323. <http://dx.doi.org/10.1007/s00161-014-0377-2>.
- Shahir, H., Mohammadi-Haji, B., Ghassemi, A., 2014. Employing a variable permeability model in numerical simulation of saturated sand behavior under earthquake loading. *Comput. Geotech.* 55, 211–223. <http://dx.doi.org/10.1016/j.compgeo.2013.09.007>.
- Skempton, A., Brogan, J., 1994. Experiments on piping in sandy gravels. *Géotechnique* 44, 449–460. <http://dx.doi.org/10.1680/geot.1994.44.3.449>.
- Sui, T., Zhang, C., Guo, Y., Zheng, J., Jeng, D.S., Zhang, J., Zhang, W., 2016. Three-dimensional numerical model for wave-induced seabed response around mono-pile. *Ships Offshore Struct.* 11, 667–678. <http://dx.doi.org/10.1080/17445302.2015.1051312>.
- Sumer, B.M., 2014. *Liquefaction Around Marine Structures*. World Scientific, New Jersey.
- Sumer, B.M., Hatipoglu, F., Fredsøe, J., Sumer, S.K., 2006. The sequence of sediment behaviour during wave-induced liquefaction. *Sedimentology* 53, 611–629. <http://dx.doi.org/10.1111/j.1365-3091.2006.00763.x>.
- Sumer, S., Sumer, B., Diken, F., Fredsøe, J., 2008. Pore pressure buildup in the subsoil under a caisson breakwater. In: *In the Eighteenth International Offshore and Polar Engineering Conference*. International Society of Offshore and Polar Engineers. pp. 664–671.
- Tian, Z., Chen, T., Yu, L., Guo, X., Jia, Y., 2019. Penetration depth of the dynamic response of seabed induced by internal solitary waves. *Appl. Ocean Res.* 90, 101867. <http://dx.doi.org/10.1016/j.apor.2019.101867>.
- Towhata, I., Sasaki, Y., Tokida, K.I., Matsumoto, H., Tamari, Y., Yamada, K., 1992. Prediction of permanent displacement of liquefied ground by means of minimum energy principle. *Soils Found.* 32, 97–116. <http://dx.doi.org/10.3208/sandf1972.32.3.97>.

- Ueng, T.S., Wang, Z.F., Chu, M.C., Ge, L., 2017. Laboratory tests for permeability of sand during liquefaction. *Soil Dyn. Earthq. Eng.* 100, 249–256. <http://dx.doi.org/10.1016/j.soildyn.2017.05.037>.
- Verruijt, A., 1969. Elastic storage of aquifers. In: *Flow Through Porous Media*. Academic Press, pp. 331–376.
- Wang, R., Cao, W., Xue, L., Zhang, J.M., 2021. An anisotropic plasticity model incorporating fabric evolution for monotonic and cyclic behavior of sand. *Acta Geotech.* 16, 43–65. <http://dx.doi.org/10.1007/s11440-020-00984-y>.
- Wang, Z., Ma, J., Gao, H., Stuedlein, A., He, J., Wang, B., 2020. Unified thixotropic fluid model for soil liquefaction. *Géotechnique* 70, 849–862. <http://dx.doi.org/10.1680/jgeot.17.P.300>.
- Wang, Z., Yang, Y., Yu, H.S., 2017. Effects of principal stress rotation on the wave-seabed interactions. *Acta Geotech.* 12, 97–106. <http://dx.doi.org/10.1007/s11440-016-0450-z>.
- Wang, B., Zen, K., Chen, G.Q., Zhang, Y.B., Kasama, K., 2013. Excess pore pressure dissipation and solidification after liquefaction of saturated sand deposits. *Soil Dyn. Earthq. Eng.* 49, 157–164. <http://dx.doi.org/10.1016/j.soildyn.2013.02.018>.
- Wang, R., Zhang, J.M., Wang, G., 2014. A unified plasticity model for large post-liquefaction shear deformation of sand. *Comput. Geotech.* 59, 54–66. <http://dx.doi.org/10.1016/j.compgeo.2014.02.008>.
- Wang, W., Zhou, M., Zhang, B., Peng, C., 2019. A dual mortar contact method for porous media and its application to clay-core rockfill dams. *Int. J. Numer. Anal. Methods Geomech.* 43, 1744–1769. <http://dx.doi.org/10.1002/nag.2930>.
- Wriggers, P., 2006. *Computational Contact Mechanics*, second ed. Springer, Berlin.
- Wu, S., Jeng, D.S., 2019. Effects of dynamic soil permeability on the wave-induced seabed response around a buried pipeline. *Ocean Eng.* 186, 106132. <http://dx.doi.org/10.1016/j.oceaneng.2019.106132>.
- Wu, S., Jeng, D.S., Seymour, B., 2020. Numerical modelling of consolidation-induced solute transport in unsaturated soil with dynamic hydraulic conductivity and degree of saturation. *Adv. Water Resour.* 135, 103466. <http://dx.doi.org/10.1016/j.advwatres.2019.103466>.
- Yamamoto, T., Koning, H., Sellmeijer, H., Hijum, E.V., 1978. On the response of a poro-elastic bed to water waves. *J. Fluid Mech.* 87, 193–206. <http://dx.doi.org/10.1017/S0022112078003006>.
- Ye, J., Jeng, D.S., 2012. Response of porous seabed to nature loadings: Waves and currents. *ASCE J. Eng. Mech.* 138, 601–613. [http://dx.doi.org/10.1061/\(ASCE\)EM.1943-7889.0000356](http://dx.doi.org/10.1061/(ASCE)EM.1943-7889.0000356).
- Ye, J., Jeng, D.S., Wang, R., Zhu, C., 2015. Numerical simulation of the wave-induced dynamic response of poro-elastoplastic seabed foundations and a composite breakwater. *Appl. Math. Model.* 39, 322–347. <http://dx.doi.org/10.1016/j.apm.2014.05.031>.
- Yin, W., Wang, W., Zhou, M., Zhang, B., 2021. Numerical evaluation of transient solar radiation effect on concrete-faced rockfill dam with dual mortar contact method. *Comput. Geotech.* 136, 104210. <http://dx.doi.org/10.1016/j.compgeo.2021.104210>.
- Young, Y.L., White, J.A., Xiao, H., 2009. Liquefaction potential of coastal slopes induced by solitary waves. *Acta Geotech.* 4, 17–34.
- Zen, K., Yamazaki, H., 1990. Mechanism of wave-induced liquefaction and densification in seabed. *Soils Found.* 30, 90–104. <http://dx.doi.org/10.3208/sandf1972.30.4.90>.
- Zhang, Y., Jeng, D.S., Gao, F., Zhang, J.S., 2013. An analytical solution for response of a porous seabed to combined wave and current loading. *Ocean Eng.* 57, 240–247. <http://dx.doi.org/10.1016/j.oceaneng.2012.09.001>.
- Zhang, S., Jia, Y., Zhang, Y., Liu, X., Shan, H., 2018b. In situ observations of wave pumping of sediments in the yellow River Delta with a newly developed benthic chamber. *Mar. Geophys. Res.* 39, 463–474. <http://dx.doi.org/10.1007/s11001-018-9344-9>.
- Zhang, J., Tong, L., Zheng, J., He, R., Guo, Y., 2018a. Effects of soil-resistance damping on wave-induced pore pressure accumulation around a composite breakwater. *J. Coast. Res.* 34, 573–585. <http://dx.doi.org/10.2112/JCOASTRES-D-17-00033.1>.
- Zhao, H.Y., Jeng, D.S., 2016. Accumulated pore pressures around submarine pipeline buried in trench layer with partial backfills. *ASCE J. Eng. Mech.* 142, 04016042. [http://dx.doi.org/10.1061/\(ASCE\)EM.1943-7889.0001093](http://dx.doi.org/10.1061/(ASCE)EM.1943-7889.0001093).
- Zhao, H.Y., Jeng, D.S., Guo, Z., Zhang, J.S., 2014. Two-dimensional model for pore pressure accumulations in the vicinity of a buried pipeline. *J. Offshore Mech. Arct. Eng. ASME* 136, 042001.
- Zhao, H., Jeng, D.S., Liao, C., Zhu, J., 2017. Three-dimensional modeling of wave-induced residual seabed response around a mono-pile foundation. *Coast. Eng.* 128, 1–21.
- Zheng, H., Liu, F., Du, X., 2015. Complementarity problem arising from static growth of multiple cracks and MLS-based numerical manifold method. *Comput. Methods Appl. Mech. Engrg.* 295, 150–171. <http://dx.doi.org/10.1016/j.cma.2015.07.001>.
- Zheng, H., Zhang, T., Wang, Q., 2020. The mixed complementarity problem arising from non-associative plasticity with non-smooth yield surfaces. *Comput. Methods Appl. Mech. Engrg.* 361, 112756. <http://dx.doi.org/10.1016/j.cma.2019.112756>.
- Zhou, M.Z., Jeng, D.S., Qi, W.G., 2020b. A new model for wave-induced instantaneous liquefaction in a non-cohesive seabed with dynamic permeability. *Ocean Eng.* 213, 107597. <http://dx.doi.org/10.1016/j.oceaneng.2020.107597>.
- Zhou, M., Liu, H., Jeng, D.S., Qi, W., Fang, Q., 2021. Modelling the wave-induced instantaneous liquefaction in a non-cohesive seabed as a nonlinear complementarity problem. *Comput. Geotech.* 137, 104275. <http://dx.doi.org/10.1016/j.compgeo.2021.104275>.
- Zhou, M., Zhang, B., Chen, T., Peng, C., Fang, H., 2020a. A three-field dual mortar method for elastic problems with nonconforming mesh. *Comput. Methods Appl. Mech. Engrg.* 362, 112870. <http://dx.doi.org/10.1016/j.cma.2020.112870>.
- Zhou, M.Z., Zhang, B.Y., Jie, Y.x., 2016b. Numerical simulation of soft longitudinal joints in concrete-faced rockfill dam. *Soils Found.* 56, 379–390.
- Zhou, M., Zhang, B., Peng, C., 2018. Numerical evaluation of soft inter-slab joint in concrete-faced rockfill dam with dual mortar finite element method. *Int. J. Numer. Anal. Methods Geomech.* 42, 781–805. <http://dx.doi.org/10.1002/nag.2768>.
- Zhou, M., Zhang, B., Peng, C., Wu, W., 2016a. Three-dimensional numerical analysis of concrete-faced rockfill dam using dual-mortar finite element method with mixed tangential contact constraints. *Int. J. Numer. Anal. Methods Geomech.* 40, 2100–2122.
- Zhou, X.L., Zhang, J., Wang, J.H., Xu, Y.F., Jeng, D.S., 2014. Stability and liquefaction analysis of porous seabed subjected to cnoidal wave. *Appl. Ocean Res.* 48, 250–265. <http://dx.doi.org/10.1016/j.apor.2014.09.005>.
- Zhu, J.F., Zhao, H.Y., Jeng, D.S., 2019. Effects of principal stress rotation on wave-induced soil response in a poro-elastoplastic sandy seabed. *Acta Geotech.* 14, 1717–1739.